GEOPHYSICS®

Q-interface imaging using accumulative attenuation estimation

Journal:	*Geophysics*
Manuscript ID	GEO-2019-0759.R2
Manuscript Type:	Technical Paper
Keywords:	2D, Q, imaging, reflection, Reverse time migration
Area of Expertise:	Seismic Inversion, Seismic Migration

Note: The following files were submitted by the author for peer review, but cannot be converted to PDF. You must view these files (e.g. movies) online.

GEO-2019-0759-table.tex

Q-interface imaging using accumulative attenuation estimation

Bei Li[1], **Yunyue Elita Li**[*1] **and Jizhong Yang**[2]

[1]*Department of Civil and Environmental Engineering*

National University of Singapore

117576 Singapore

[2]*Formerly Department of Civil and Environmental Engineering*

National University of Singapore

117576 Singapore

Presently State Key Laboratory of Marine Geology

Tongji University

200092 Shanghai

[*]*ceeliyy@nus.edu.sg*

(July 24, 2020)

Running head: **Q-interface imaging**

ABSTRACT

A high-resolution Q model is beneficial for more accurate attenuation compensation and preferable for gas-related interpretation. Given an accurate velocity model, viscoacoustic/viscoelastic full waveform inversion (Q-FWI) could reconstruct a high-resolution Q model, but it requires significant computational cost due to the iterative process of solving viscoacoustic/viscoelastic wave equations. We propose an efficient high-resolution Q-

interface imaging method through the following steps. First, we estimate the attenuated traveltime via inversion of the dynamic match filter between synthetic acoustic and observed viscoacoustic prestack records. Second, we derive virtual Q reflectivities via piecewise linear regression on the attenuated traveltime estimations. Finally, by convolving a source wavelet on the virtual Q reflectivities, we generate the virtual Q reflection gathers and migrate them through reverse time migration (RTM) to image the Q interfaces. The Q-interface information is essentially derived by comparing the accumulative attenuation effects estimated from near-offset primary reflections arriving at the same receiver successively in time, and the high resolution is assured by the piecewise linear regression based on the prior knowledge of the Q-interface number along depth. The key insight of our method is to use accumulative attenuation effects to derive immediate effects of Q interfaces (virtual Q reflections) in the prestack data domain, which are readily applicable for Q-interface imaging through simple acoustic RTM. Numerical examples demonstrate that our method produces unprecedented high-resolution images of Q interfaces along the vertical direction with satisfying positioning and interpretable polarity.

INTRODUCTION

Anelasticity causes conversion from kinetic energy to heat during seismic wave propagation, resulting in both amplitude decay and phase distortion of the seismic waveforms. Such property of the subsurface media is generally referred to as seismic intrinsic attenuation, which is normally quantified by the quality factor Q. During seismic data processing and inversion, Q should be considered so that the Q effects can be compensated for better retrieving the elastic properties, such as P- and S-wave velocities (e.g., Wang, 2002; Fletcher et al., 2012; Dutta and Schuster, 2014; Guo and McMechan, 2018; Xue et al., 2018). Additionally, the Q value itself is closely related to pore fluid properties (e.g., Müller et al., 2010), indicating that Q can also be an interpretable attribute for fluid saturation, especially gas saturation (e.g., Qi et al., 2017). A high-resolution Q model is advantageous for more accurate compensation and meaningful interpretation, especially when large Q contrasts exist. A low-Q anomaly often indicates gas pockets (e.g., Shen et al., 2018), and the boundary information of the low-Q zone is helpful for locating gas pockets more accurately and even approximate the reserve volume. Furthermore, delineation of the low-Q anomaly could also improve the monitoring of CO_2 transportation during sequestration (e.g., Zhu et al., 2017).

Currently the most commonly-used Q model building technique is Q tomography (e.g., Quan and Harris, 1997; Dutta and Schuster, 2016). However, it generally fails to provide a high-resolution result, since it only utilizes transmissive or accumulative attenuation effects by directly projecting the estimation residual along corresponding ray- or wave-paths. Viscoacoustic/viscoelastic full waveform inversion (Q-FWI) (e.g., Kamei and Pratt, 2013; Stopin et al., 2016) has the potential to take the immediate or reflective attenuation effects into account for retrieving the high-wavenumber Q model components, provided that the accurate velocity model has been reconstructed. Nonetheless, the computational cost for Q-FWI can be prohibitive in real applications, since it requires to iteratively solve the viscoacoustic/viscoelastic wave equations (e.g., Carcione et al., 1988; Zhu and Harris, 2014), which generally costs more than acoustic/elastic wave-equation modeling.

An efficient high-resolution strategy is the migration or imaging technique, which has been widely used for resolving wave-impedance interfaces by "relocating" the reflections generated from those interfaces to their corresponding spatial locations based on imaging conditions (e.g., Claerbout, 1971; French, 1975; Stoffa et al., 1990; McMechan, 1983). Hence, a high-resolution Q-interface image intuitively should be achieved by migrating the reflections caused by Q contrasts. However, such Q reflections are practically impossible to explicitly separate from the overwhelming reflections generated by wave-impedance contrasts and simultaneously attenuated by background Q. Contrary to the difficulty of retrieving the immediate attenuation effects (as Q reflections), the accumulative attenuation effects (as effective Q) along the entire wave-path is relatively easy and practical to estimate, e.g., based on the changes of amplitude spectra of the attenuated waveforms, such as amplitude spectral ratio (e.g., Toksoz et al., 1979; Brzostowski and McMechan, 1992) or centroid/peak frequency shift (e.g., Quan and Harris, 1997; Hu et al., 2011). Hence, Q-interface imaging based on estimated accumulative attenuation effects is favorable. Lin et al. (2018) quantify cumulative attenuation effects using the instantaneous frequency (approximating the centroid frequency) in the data domain. Then, they directly migrate the estimated instantaneous frequency to the image domain, followed by the calculation of the first-order derivative along depth. Such implementation intends to attribute effective-Q contrasts to their corresponding velocity-interface positions in the image domain, but it generates apparent velocity-interface imprints due to neglecting the estimation gaps of the instantaneous frequencies between adjacent reflections.

In this study, we propose a Q-interface imaging method, which infers the immediate attenuation effects from the accumulative attenuation effects estimated in the prestack data domain. We employ the attenuated traveltime (e.g., Cavalca et al., 2011) to quantify the accumulative attenuation effects, and point out that for near-offset recordings the attenuated traveltime should be piecewise linear along traveltime. This piecewise linear feature is utilized as precondition at two sequential data-domain inversion steps: first, attenuated traveltime estimation through matching the synthetic acoustic with the observed viscoacoustic waveforms; second, the virtual Q reflectivity derivation via piecewise linear regression. Essentially, the immediate effects of Q contrasts (virtual Q reflectivities) are obtained by comparing the accumulative attenuation effects (the attenuated traveltime) estimated from adjacent near-offset primary reflective wave-paths. With the prior knowledge of Q-interface number along depth, the piecewise linear regression provides accurate and robust virtual Q reflectivities against both the inevitable errors in the attenuated traveltime estimations and possible mismatch between the Q interfaces and the velocity interfaces. Convolving the virtual Q reflectivities with a source wavelet, we generate the virtual Q reflections, which are then directly inputted to the reverse time migration (RTM) for Q-interface imaging. To the best of our knowledge, our Q-interface imaging method is the first to achieve Q-anomaly identification with a high vertical resolution, satisfying depth positioning, and meaningful Q-contrast interpretation.

This major contribution stems from a new insight that the Q-interface information can be extracted from the accumulative attenuation estimations in the prestack data domain, which does not require iterative wave propagation simulation. Physically, this extraction is possible because of the piecewise linear property of the accumulative attenuation effects along traveltime. Practically, the high resolution achieved by our method is based on the prior knowledge of the expected number of Q interfaces along depth, which defines our piecewise linear regression.

The structure of this paper is as follows: first, we show the definition of the attenuated traveltime and point out its connection with the immediate effects of Q interfaces in the data domain; second, we develop the match-filter-based attenuated-traveltime estimation; third, we propose the piecewise linear regression and its following procedures to generate the virtual Q reflections fed to RTM for Q-interface imaging; fourth, we provide two synthetic examples to demonstrate the effectiveness and robustness of our method; and finally, we discuss the limitations of our method and future work assumed.

METHODOLOGY

The attenuated traveltime and the Q interface

The attenuated traveltime $\Psi(t)$ is defined by Cavalca et al. (2011) as

$$\Psi(t) = \int_0^t Q^{-1}(\tau) d\tau, \tag{1}$$

where t denotes the total traveltime of waves propagating along any given wave-path; $Q^{-1}(\tau)$ represents the dissipation factor at a given moment τ along the wave-path. As the integration of dissipation factor along the whole wave-path, $\Psi(t)$ indicates the cumulative attenuation. Here, we seek a direct link between $\Psi(t)$ and the Q interface in heterogeneous Q media.

Taking the second-order time derivative on both sides of equation 1, we have

$$\Psi''(t) = (Q^{-1})'(t), \tag{2}$$

equation 2 indicates that $\Psi''(t)$ represents the change of the dissipation factor with respect to traveltime. In the transmission regime, $\Psi''(t)$ highlights the variation of Q^{-1} along a single wave-path. In the reflection regime, $\Psi''(t)$ indicates the variation of Q^{-1} across adjacent wave-paths arriving at the same receiver successively.

Based on a simple layered model, Figure 1 illustrates the relationship between the attenuated traveltime and the Q interface in the reflection regime. It shows that for blockwise constant heterogeneous Q, $\Psi(t)$ for primary reflective wave-paths is approximately piecewise linear within relatively small offset range, and $\Psi'(t)$ represents the local Q^{-1}. Consequently, $\Psi''(t)$ is sparse, where spike positions represent the Q-interface positions along traveltime and spike amplitudes are proportional to the difference of Q^{-1} on both sides of Q interfaces. Thus, $\Psi''(t)$ can be viewed as the virtual Q reflectivity. By convolving $\Psi''(t)$ with a source wavelet, we can synthesize the virtual Q reflections. Such virtual Q reflections kinematically resemble the theoretical reflections caused by Q interfaces, and dynamically represent Q^{-1} contrasts. Therefore, we can directly utilize these virtual Q reflections for Q-interface imaging through RTM with the assistance of a migration velocity model. When the migration velocity is kinematically accurate, we obtain high resolution Q-interface images that reflect the true Q^{-1} contrasts in depth. Notice that the derivations leading to virtual Q reflections are based on accumulative attenuation estimations, which could be purely data-driven and independent of the migration velocity model. Hence, the key here is to derive the virtual Q reflectivity accurately and efficiently from the data domain.

Match-filter-based attenuated traveltime estimation

To calculate $\Psi''(t)$, a high-resolution $\Psi(t)$ must be estimated from the observed viscoacoustic waveform. We revise the match-filter-based Q estimation in the data domain (Cheng and Margrave, 2012) for $\Psi(t)$ estimation, which is achieved via the minimization of the mismatch between the forward-Q-filtered synthetic acoustic waveform with the observed viscoacoustic waveform

$$\min_{\Psi_{s,r,t}} \|u(x_s, x_r, t; \Psi_{s,r,t}) - d_{s,r,t}\|_2^2, \tag{3}$$

where $\Psi_{s,r,t}$ denotes $\Psi(x_s, x_r, t)$ which is the attenuated traveltime defined in the prestack data domain as x_s, x_r, and t representing source locations, receiver locations, and the traveltime, respectively; $d_{s,r,t}$ denotes $d(x_s, x_r, t)$ which is the observed viscoacoustic record, and $u(x_s, x_r, t; \Psi_{s,r,t})$ is the forward-Q-filtered record given synthetic acoustic record $R(x_s, x_r, t)$ and $\Psi_{s,r,t}$:

$$u(x_s, x_r, t; \Psi_{s,r,t}) = \frac{1}{2\pi} \int \tilde{R}(x_s, x_r, \omega) \exp[i\omega(\ln(i\omega/\omega_0)\Psi_{s,r,t} + t)] d\omega, \tag{4}$$

in which,

$$\tilde{R}(x_s, x_r, \omega) = \int R(x_s, x_r, t) \exp(-i\omega t) dt, \tag{5}$$

with i the imaginary unit, ω the angular frequency, ω_0 the reference angular frequency, and $\tilde{R}(x_s, x_r, \omega)$ the synthetic acoustic record in the frequency domain (see Appendix A for details about the derivation of forward Q filtering). In this study, we assume an accurate velocity model is available to synthesize the accurate acoustic record, and its corresponding reference frequency is known to perform the forward Q filtering.

To solve for $\Psi_{s,r,t}$ using the gradient descent algorithm, we first linearize the inversion problem shown in equation 3 as follows:

$$\min_{\delta\Psi_{s,r,t}} \|W^{(i)}\mathbf{J}_{\Psi}^{(i)}\delta\Psi_{s,r,t} - (d_{s,r,t} - W^{(i)}u_{s,r,t}^{(i)})\|_2^2, \tag{6}$$

in which,

$$\Psi_{s,r,t}^{(i+1)} = \Psi_{s,r,t}^{(i)} + \delta\Psi_{s,r,t}, \tag{7}$$

$$u_{s,r,t}^{(i)} = u(x_s, x_r, t; \Psi_{s,r,t}^{(i)}), \tag{8}$$

$$\mathbf{J}_{\Psi}^{(i)} = \frac{\partial u_{s,r,t}}{\partial \Psi_{s,r,t}}|_{\Psi_{s,r,t}=\Psi_{s,r,t}^{(i)}}. \tag{9}$$

where $\Psi_{s,r,t}^{(i)}$ represents the attenuated traveltime model at the ith linearization step (for $i = 0$, we initialize the inversion as $\Psi_{s,r,t}^{(0)} = 0$ in this study), and $\delta\Psi_{s,r,t}$ is the model increment we solve for at current linearization step; $u_{s,r,t}^{(i)}$ denotes the filtered synthetic acoustic record given $\Psi_{s,r,t}^{(i)}$; $W^{(i)}$ denotes a windowed normalizing operator, which is used to eliminate the amplitude scaling difference between $d_{s,r,t}$ and $u_{s,r,t}^{(i)}$ within each window; $W^{(i)}$ also performs as an adaptive weighting on the data residual; $\mathbf{J}_{\Psi}^{(i)}$ denotes the Jacobian matrix given $\Psi_{s,r,t}^{(i)}$. It is a diagonal matrix with the size of $N_d \times N_d$, where N_d represents total number of data samples. The diagonal entries of the whole Jacobian matrix does not require much memory, since we can calculate them while applying them trace-by-trace (see Appendix A for details about the calculation of $\frac{\partial u_{s,r,t}}{\partial \Psi_{s,r,t}}$).

Secondly, we employ two chained preconditioning steps, including linear interpolation L and smoothing G, to accelerate the convergence to a suitable attenuated traveltime model:

$$\delta\Psi_{s,r,t} = GLp_{s,r,t_s}, \tag{10}$$

where p_{s,r,t_s} denotes $p(x_s, x_r, t_s)$, which is the sampled $\delta\Psi_{s,r,t}$ model at t_s, picked at the envelope peaks of strong primary reflections in $u_{s,r,t}$. The linear interpolation operator L is applied along t direction to reconstruct $\delta\Psi_{s,r,t}$ from p_{s,r,t_s} for the continuous waveform assuming the Q model is blockwise constant. Then we apply the smoothing operator G defined in (x_s, x_r, t) domain (see Appendix B for details about the smoothing operator). The smoothing operator is designed to honor the similarity of the estimated attenuated traveltime from nearby primary reflective wave-paths, such that the attenuated traveltime estimation is robust against the influence from multiples and diffractions whose wave-paths and hence attenuation effects are drastically different in comparison to the neighboring primary reflections.

Finally, the attenuated traveltime along each trace should be generally increasing with t because the wave energy arriving later probably experiences more attenuation. Therefore, we incorporate an inequality model regularization to penalize the decrease of $\Psi_{s,r,t}$ along t. Together with the preconditioning shown in equation 10, the linearized inversion problem becomes

$$\min_{p_{s,r,t_s}} \|W^{(i)}\mathbf{J}_{\Psi}^{(i)}GLp_{s,r,t_s} - (d_{s,r,t} - W^{(i)}u_{s,r,t}^{(i)})\|_2^2 + \epsilon R_s(D(\Psi_{s,r,t}^{(i)} + GLp_{s,r,t_s})), \tag{11}$$

where D represents the negative first-order differencing operator along t; R_s denotes the smooth rectifier linear unit (SmoothReLU) function, $R_s(x) = \ln(1+\exp(x))$, which penalizes the positive residual but passes the negative residual in a soft clipping manner.

Equation 11 solves for p_{s,r,t_s}, which then will be used to update $\Psi_{s,r,t}$ via equation 10 and 7. By re-linearization using the updated $\Psi_{s,r,t}$, we iteratively solve this nonlinear problem shown in equation 3, which eventually provides us the attenuated traveltime estimation in the prestack data domain.

Piecewise linear regression

After the attenuated traveltime estimation, we ideally can derive the virtual Q reflectivity by taking the second-order differencing on $\Psi_{s,r,t}$ along t. However, such direct calculation tends to amplify the errors in the estimated $\Psi_{s,r,t}$. Moreover, according to equation 10, the "anchors" of $\Psi_{s,r,t}$ being effectively estimated are at the sample time t_s, whereas the other parts of $\Psi_{s,r,t}$ are essentially obtained by linear interpolation and smoothing on p_{s,r,t_s}. Therefore, a direct second-order differencing on $\Psi_{s,r,t}$ implicitly assumes that the Q interface must be co-located with a velocity interface, whose primary reflection corresponds to a certain picked t_s. However, the real Q-interface positions may not be included in t_s, due to practical situations, such as low SNR and different gas-saturation sensitivity of the velocity and Q.

To stably derive the virtual Q reflectivity and relax the assumption of co-location between Q and picked velocity interfaces, we propose a piecewise linear regression process on the attenuated traveltime estimation sampled at t_s, i.e., $\Psi_{s,r,t_s} = S\Psi_{s,r,t}$, where S is the sampling operator. It is another inversion problem for the turning positions $\mathbf{T}_{s,r} = [T_{(s,r)0}, T_{(s,r)1}, \cdots, T_{(s,r)N+1}]^T$ and slopes $\mathbf{B}_{s,r} = [B_{(s,r)0}, B_{(s,r)1}, \cdots, B_{(s,r)N}]^T$ of the piecewise linear function with $N+1$ pieces defined along all traces. The inversion is achieved by matching the predicted piecewise linear attenuated traveltime samples with the estimated attenuated traveltime samples:

$$\min_{\mathbf{m}_{s,r}} \| S\Phi(x_s, x_r, t; \mathbf{m}_{s,r}) - \Psi_{s,r,t_s} \|_2^2, \tag{12}$$

where $\mathbf{m}_{s,r} = (\mathbf{T}_{s,r}, \mathbf{B}_{s,r})$; $\Phi(x_s, x_r, t; \mathbf{m}_{s,r})$ is the predicted piecewise linear attenuated traveltime given $\mathbf{m}_{s,r}$.

Based on the prior knowledge of the piecewise linear attenuated traveltime including: (1)

zero initial condition, i.e., $\Phi(x_s, x_r, 0) = 0$, and (2) the number of pieces $N+1$ determined by the expected number of Q interfaces along depth, we can formulate the predicted piecewise linear attenuated traveltime as follows:

$$\Phi(x_s, x_r, t; \mathbf{m}_{s,r}) = \sum_{i=0}^{j-1} (T_{(s,r)i+1} - T_{(s,r)i}) B_{(s,r)i} + (t - T_{(s,r)j}) B_{(s,r)j}, \tag{13}$$

$$T_{(s,r)j} \leq t < T_{(s,r)j+1},\ j = 0, 1, \cdots, N,$$

where $T_{(s,r)0}$ and $T_{(s,r)N+1}$ denote the zero and the maximum recording time, respectively, whereas $T_{(s,r)1}$ to $T_{(s,r)N}$ indicate the Q-interface positions in between; $B_{(s,r)0}$ to $B_{(s,r)N}$ represent Q^{-1} for different blocks divided by $\mathbf{T}_{s,r}$ in the data domain, and consequently Q^{-1} for different Q layers in the image domain.

To solve this nonlinear problem shown in equation 12, we first linearize it as follows:

$$\min_{\delta \mathbf{m}_{s,r}} = \| S \mathbf{J}_{\mathrm{P}}^{(i)} \delta \mathbf{m}_{s,r} - (\Psi_{s,r,t_s} - S \Phi_{s,r,t}^{(i)}) \|_2^2, \tag{14}$$

in which,

$$\mathbf{m}_{s,r}^{(i+1)} = \mathbf{m}_{s,r}^{(i)} + \delta \mathbf{m}_{s,r}, \tag{15}$$

$$\Phi_{s,r,t}^{(i)} = \Phi(x_s, x_r, t; \mathbf{m}_{s,r}^{(i)}), \tag{16}$$

$$\mathbf{J}_{\mathrm{P}}^{(i)} = \frac{\partial \Phi_{s,r,t}}{\partial \mathbf{m}_{s,r}} |_{\mathbf{m}_{s,r} = \mathbf{m}_{s,r}^{(i)}}, \tag{17}$$

where $\mathbf{m}_{s,r}^{(i)}$ represents the model at the ith linearization step, and $\delta \mathbf{m}_{s,r}$ is the model increment we seek; and $\Phi_{s,r,t}^{(i)}$ and $\mathbf{J}_{\mathrm{P}}^{(i)}$ denote currently predicted piecewise linear attenuated traveltime and the Jacobian matrix given $\mathbf{m}_{s,r}^{(i)}$, respectively. The Jacobian matrix is a block-diagonal matrix with the size of $N_d \times (2N+1) \cdot N_r$, where N_r is the total number of traces in the data domain. For predicted attenuated traveltime Φ along each trace, the derivative shown in equation 17 is only related to T and B at that particular trace. Therefore, the Jacobian matrix is calculated while being applied trace-by-trace without requiring any significant memory (total $2N+1$ calculation of derivatives at each time sample along each trace).

Since the estimated $\Psi_{s,r,t}$ is generally smooth in the prestack data domain, it is reasonable for us to apply preconditioning that maintains the smoothness of turning positions and slopes across adjacent traces. Thus, we can precondition $\delta\mathbf{m}_{s,r}$ as follows:

$$\delta\mathbf{m}_{s,r} = H\mathbf{q}_{s,r}, \tag{18}$$

where $\mathbf{q}_{s,r}$ denotes the raw model increment of $\mathbf{m}_{s,r}$, and H is the smoothing operator along both x_s and x_r directions (see Appendix B for details about the smoothing operator).

Substituting equation 18 into 14, we solve this linearized preconditioned inversion problem for $\delta\mathbf{m}_{s,r}$, which is then used to update $\mathbf{m}_{s,r}$ via equation 15, followed by re-linearization using the updated $\mathbf{m}_{s,r}$. Eventually, we obtain the optimal $\mathbf{T}_{s,r}$ and $\mathbf{B}_{s,r}$ that generate the piecewise linear attenuated traveltime that matches the attenuated traveltime estimation samples best.

Now using the optimal $\mathbf{T}_{s,r}$ and $\mathbf{B}_{s,r}$, we can calculate the virtual Q reflectivity $r(x_s, x_r, t)$ as follows:

$$r(x_s, x_r, t) = \begin{cases} B_{(s,r)j} - B_{(s,r)j-1}, & \text{for} \quad t = T_{(s,r)j} \\ 0, & \text{for} \quad t \neq T_{(s,r)j} \end{cases}, \; j = 1, 2, \cdots, N, \tag{19}$$

which provides both kinematic and contrast information of the Q interfaces in the data domain.

It is possible to combine the match-filter-based attenuated traveltime estimation and the piecewise linear regression together, by taking the latter as strong preconditioning for the former. However, the nonlinearity of such an optimization problem will be more severe, easily trapping the inversion within local minima. Therefore, we choose to perform these two inversion processes sequentially for a more accurate and stable derivation of the virtual Q reflectivity.

After retrieving the virtual Q reflectivity, we convolve a source wavelet on $r(x_s, x_r, t)$, generating the virtual Q reflections. Then, we feed them to acoustic RTM based on the smoothed velocity model for imaging Q interfaces with high resolution and satisfying positioning. Moreover, since $r(x_s, x_r, t)$ also indicates the contrast of Q^{-1} on both sides of a Q interface, the polarity of our obtained Q-interface image can also be interpreted as the attenuation changes along depth.

NUMERICAL EXAMPLES

We use two synthetic examples to illustrate the procedure and demonstrate the effectiveness and robustness of our Q-interface imaging method. The first example is a simple layered velocity model with a rectangular low-Q anomaly in the middle. The second example is a more realistic gas chimney model. Model discretization and acquisition configuration for these two examples are shown in Table **??**. The viscoacoustic waveforms in these examples are synthesized by solving the fractional-Laplacian wave equation (Zhu and Harris, 2014) through its low-rank approximation (Fomel et al., 2013). As for the corresponding acoustic record used in the match-filter-based attenuated traveltime estimation, we generate them through solving the scalar wave equation with the accurate velocity model. The Q models in both examples are isolated low-Q anomaly structures, which means vertically there are two Q interfaces corresponding to the top and bottom boundaries of the low-Q anomaly. Hence, $N = 2$ for piecewise linear regression in both examples.

Layered model

Firstly, we test our method on simple layered velocity and Q models, as shown in Figure 2. The top boundary of the Q-anomaly is not co-located with any of the velocity interfaces, whereas the bottom boundary coincides with a velocity interface.

Figure 3 shows the synthetic acoustic and viscoacoustic waveforms for the shot gather at $x_s = 1000$ m. In both seismograms, we can see the direct arrivals and nine primary reflections corresponding to the nine velocity interfaces shown in Figure 2a. The viscoacoustic seismogram shows noticeably weaker amplitude than the acoustic seismogram starting from the third primary reflection since the low-Q anomaly begins above the third velocity interface. Although less obvious, the phase distortion of the viscoacoustic waveform in comparison with the acoustic waveform is actually severe, especially for deeper reflections. Both the amplitude decay and phase distortion shown in Figure 3 are considered by our match-filter-based attenuated traveltime estimation.

We remove the first arrivals and restrict the offset range within 400 m for the attenuated traveltime estimation. Here, the offset range is a subjective choice balancing the accuracy and computational cost. In practice, one may choose relatively large offset for the sequential inversion processes in view of available computational power. When applying the generated virtual Q reflections to RTM, we can test different offset truncation and choose the optimal offset range according to the final Q-interface image quality. Figure 4 presents the attenuated traveltime estimation in the zero-offset gather and two sample common shot gathers at $x_s = 600$ m and 1000 m. Estimations shown in different domains are generally smooth along x_s and x_r, and almost monotonically increasing in t, honoring the prior knowledge enforced by the preconditioning and regularization shown in equation 11.

To further validate the estimation, Figure 5 provides waveform comparison for the sample trace at $x_r = 1100$ m from the common shot gather at $x_s = 1000$ m. The filtered acoustic waveform (blue curve) via equation 4 based on $\Psi(x_s = 1000 \text{ m}, x_r = 1100 \text{ m}, t)$ shown in Figure 4c achieves satisfying consistency with the viscoacoustic waveform (red curve), indicating that the data residual has been reduced significantly through the match-filter-based inversion process.

After the match-filter-based attenuated traveltime estimation, the piecewise linear regression is performed on the estimation samples Ψ_{s,r,t_s}. In Figure 6, we display the initial and the inverted turning positions $\mathbf{T}_{s,r}$ and slopes $\mathbf{B}_{s,r}$ in the zero-offset gather. We initialize $T_{(s,r)1} \approx 700$ ms and $T_{(s,r)2} \approx 900$ ms based on a rough read of the estimation shown in Figure 4a. Then, we initialize $\mathbf{B}^{(0)}_{s,r}$ as

$$B^{(0)}_{(s,r)j} = \frac{\Psi(x_s, x_r, T^{(0)}_{(s,r)j+1}) - \Psi(x_s, x_r, T^{(0)}_{(s,r)j})}{T^{(0)}_{(s,r)j+1} - T^{(0)}_{(s,r)j}},\ j = 0, 1, \cdots, 2. \tag{20}$$

From the inverted $\mathbf{B}_{s,r}$ shown in Figure 6b, it is easy to identify the horizontal span of the low-Q anomaly between 560 m and 1440 m, defined by 3dB bandwidth of the inverted $B_{(s,r)1}$. It demonstrates fair horizontal sensitivity of zero-offset estimation that any conventional Q-model building method may pick up. Nonetheless, delineating the vertical boundaries of the Q anomaly is much more challenging. In our study, such boundaries are indicated by the inverted turning positions $T_{(s,r)1}$ and $T_{(s,r)2}$. Furthermore, the slopes $B_{(s,r)0}$, $B_{(s,r)1}$, and $B_{(s,r)2}$ provide the dissipation factors, Q^{-1}, for the background ($B_{(s,r)0}$ and $B_{(s,r)2}$ are both around 1/100) and the low-Q anomaly ($B_{(s,r)1}$ is around 1/20).

To validate the piecewise linear regression results, Figure 7 shows the regressed function for the same sample trace ($x_s = 1000$ m, $x_r = 1100$ m) as shown in Figure 5. The regressed piecewise linear function (blue line) has honored the estimation samples $\Psi(x_s =$

1000 m, $x_r = 1100$ m, t_s) (red dots) well. Note that the predicted top boundary position (left blue circle) is in the middle of the second and third primary reflections, whereas the predicted bottom boundary position (right blue circle) is co-located with the fifth primary reflection. This is consistent with the relationship between the positions of the low-Q anomaly and the velocity interfaces in the reference models (Figure 2).

According to the inverted $\mathbf{T}_{s,r}$ and $\mathbf{B}_{s,r}$, we can derive the virtual Q reflectivity via equation 19, and then generate the virtual Q reflection gathers by convolving a source wavelet. Figure 8 shows the virtual Q reflections for the common shot gathers at $x_s = 600$ m and 1000 m, corresponding to the attenuated traveltime estimation shown in Figure 4b and 4c, respectively. Both events in the given virtual Q reflection gathers represent the kinematics of reflections as if they were generated from the top and bottom boundaries of the low-Q anomaly. The polarity reversal between the two events represents the increase and decrease of Q^{-1} across the top and bottom Q boundaries, respectively. In comparison with $x_s = 1000$ m, which is right in the middle of the low-Q anomaly, the virtual Q reflection gather at $x_s = 600$ m shows apparent amplitude variation along x_r direction, since it is near the left edge of the low-Q zone. The virtual Q reflections away from the low-Q zone are unreliable, which is largely dependent on the initial solution of the piecewise linear regression. However, these unreliable virtual Q reflections are relatively weak, which only create minor artifacts near the left and right boundaries of the Q anomaly in the stacked image.

Here, we migrate virtual Q reflection gathers using the acoustic RTM based on a smoothed accurate velocity model. The obtained Q-interface image is displayed and compared with the reference Q model in Figure 9. Figure 10 further presents a trace comparison between the image and the reference model, at the distance of 1200 m. In view of the top and bottom Q boundaries, the imaged Q interfaces are properly positioned with high resolution and interpretable polarities, no matter whether they are overlapped with velocity interfaces. Notice that the Q^{-1} interfaces along depth are not totally sharp boundaries. Instead, the Q^{-1} changes along depth gradually within 50 m, representing the dispersive situation of the Q interfaces. We can see that the two major events in our obtained Q-interface image approximately focus at the middle of the 50 m Q^{-1} change.

Gas chimney model

To test our method in a more realistic situation, we employ the gas chimney model, which consists of more complex velocity and Q structures, as shown in Figure 11. The low-Q anomaly in the Q model has some fingering structures near the left and right edges of the low-Q anomaly. The velocity model, in comparison to the simple layered one, contains moderate horizontal variation caused by the low-velocity anomaly within a similar area of the low-Q zone.

In Figure 12, we compare the acoustic and viscoacoustic seismograms for the shot gather at $x_s = 1200$ m. Strong diffractions are abundant in both seismograms. Hence, apart from muting direct arrivals and truncating data into limited offset range (400 m) and time range (1200 ms), we also apply f-k filtering in common offset domain to suppress the diffractions as preprocessing. Figure 13 shows the zero-offset gathers for both acoustic and viscoacoustic seismograms before and after f-k filtering. Comparing the seismograms vertically, we can see that most of the strong diffractions are removed by simple f-k filtering. However, there are still visible diffractions remaining in the data. To investigate the effect of different amounts of diffractions, we perform the match-filter-based attenuated traveltime estimation and the piecewise linear regression on both seismograms before and after f-k filtering.

Figure 14 shows the zero-offset results of these two sequential inversion processes for both situations shown in Figure 13. It appears that strong diffractions markedly deteriorate the estimation of the attenuated traveltime, and consequently make the following piecewise linear regression unreliable. However, with relatively weak diffractions, the inversion results shown in Figure 14c and 14d are greatly improved in comparison with those shown in Figure 14a and 14b. From Figure 14d, the vertical and horizontal extent of the low-Q anomaly are captured by the inverted $\mathbf{T}_{s,r}$ and $\mathbf{B}_{s,r}$. The background Q is corresponding to $B_{(s,r),0}$ and $B_{(s,r),2}$, which are approximately 1/100. The middle part of $B_{(s,r)1}$ is around 1/20, indicating the dissipation factor of the low-Q zone. From the 3dB bandwidth of the inverted $B_{(s,r)1}$ shown in Figure 14d, we interpret the horizontal span of the Q anomaly as between 800 m and 1550 m. We compare the inversion results at a sample trace ($x_s = 1300$ m, $x_r = 1300$ m) in Figure 15. It further demonstrates that after simple f-k filtering, the inversion processes are able to fit the waveforms (Figure 15c) and the estimated attenuated traveltime samples (Figure 15d) better.

In Figure 16, we compare the final Q-interface images obtained from seismograms with and without f-k filtering. The image obtained from the data with strong diffractions (Figure 16a) shows severe mispositioning, especially of the Q-anomaly bottom boundary. This is because the attenuation estimation is affected more by diffractions than by primary reflections as the trevaltime increases, resulting in unreasonable piecewise linear regression and thus the poor image for the bottom boundary. The final image obtained from data after f-k filtering (Figure 16b) is fairly consistent with the reference model, despite the existence of some remaining diffractions as shown in Figure 13c and 13d. In Figure 17, we compare the two sampled image traces at the distance of 1300 m with the reference Q^{-1} model trace. It shows that the positioning of both the top and bottom boundaries are reasonably accurate after f-k filtering.

In addition to diffractions, random noise is another major practical concern when performing attenuation estimation. Here, we conduct tests with different signal-to-noise ratio (SNR) by adding Gaussian random noise $n \sim N(0, \sigma_n)$. Figure 18 shows two zero-offset gathers of the normalized viscoacoustic data adding random noise with $\sigma_n = 0.005$ and 0.01, respectively. The preprocessing includes first-arrival muting and f-k filtering. Because data amplitude decreases as traveltime and attenuation increases, the SNR when $\sigma_n = 0.005$ decreases from 6.7 around 400 ms to 0.3 around 900 ms. When $\sigma_n = 0.01$, the SNR is 1.6 around 400 ms and 0.1 around 900 ms. These test cases represent realistic field data scenarios even after standard bandpass filtering below 65 Hz.

Figure 19 compares the inversion results for the zero-offset gather using the two noisy viscoacoustic data. Compared to the noiseless results in Figure 14c and 14d, the estimated attenuated traveltime map becomes noisier as SNR decreases. Moreover, the estimation of the absolute attenuated traveltime becomes worse. Nonetheless, both the lateral and vertical extent of the Q-anomaly can still be interpreted from the inversion results of the noisy data. Figure 20 further displays the sample trace ($x_s = 1300$ m, $x_r = 1300$ m) inversion results. Although the waveform misfit after the match-filter-based inversion is large in amplitude, the attenuated traveltime estimation and thus the piecewise linear regression are barely affected in Figure 20a and 20b. However, with more random noise, Figure 20d shows that the attenuation is underestimated and the regressed turning positions are shifted towards shallower depths.

In Figure 21a and 21b, we display the final Q-interface images obtained from the noisy data with $\sigma_n = 0.005$ and 0.01, respectively. When SNR is large, Q-interface image shown in Figure 21a is qualitatively the same as the noiseless image in Figure 16b, and shows satisfying delineation of the Q-anomaly horizontal boundaries. As SNR further degrades, the image shown in Figure 21b locates the horizontal boundaries shallower than their reference depths, which is consistent with the results shown in Figure 19d and Figure 20d. Figure 22 displays the image trace comparison with the reference model. It demonstrates that accurate vertical positioning and superior resolution can be achieved with moderate amount of noise. When the data SNR is too low, our algorithm can still produce high-resolution delineation of the Q-anomaly, albeit with underestimated depths.

DISCUSSION

The tests provided in the gas chimney model demonstrate that our Q-interface imaging method is robust against a reasonable amount of noise, including temporal-correlated noise, such as diffractions, and uncorrelated noise, such as Gaussian random noise. The robustness mainly comes from the preconditioning and regularization shown in equation 11. They can facilitate the attenuation estimation in the prestack data domain against the noise essentially by the smoothing constraint since the noises attenuate disparately in comparison with the nearby primary reflections. However, if the coherent noise in the data overwhelms primary reflections, the imaging result will be negatively affected in terms of the Q-interface positioning and focusing. Therefore, we recommend removing any coherent noise as much as possible before applying the Q-interface imaging method.

From the numerical examples, we can see that the top boundary of the low-Q anomaly is generally better imaged than the bottom boundary. This can be explained from the following three perspectives. First, from the perspective of attenuation estimation, as the wave propagates through the low-Q zone and losses more energy, there is lower SNR and thus a higher chance for estimation error at the deeper Q interface. Second, in terms of piecewise linear regression, since the subsurface velocity normally increases with depth, the temporal error of the deeper turning position from piecewise linear regression will be generally amplified more than that of the shallower turning position during migration. Finally, from a pure migration point of view, the deeper Q interface has smaller offset illumination due to the relatively limited offset range. Nonetheless, with all tested examples, the proposed Q-interface imaging workflow archives much higher resolution of the lower boundary of the Q-anomaly compared to conventional Q-tomography methods.

To enable the key step of the attenuated traveltime estimation, our match-filter-based inversion needs accurate acoustic records as a reference, which are simulated based on the accurate velocity model in this study. Nonetheless, it is possible to generate sufficiently reliable acoustic records using only a smooth velocity model and a smooth Q model, both of which can be obtained by conventional tomography. Based on these smoothed models, we could perform Q-compensated least-squares RTM (e.g., Dutta and Schuster, 2014; Guo and McMechan, 2018) and generate the reference acoustic records through Born modeling. When velocity error is relatively large, model extensions for least-squares RTM (e.g., Sun et al., 2015) can be utilized to ensure a good data recovery. Besides, the proposed method also has the potential to be purely data-based by replacing current match-filter-based attenuated traveltime estimation by classic data-domain Q estimation strategies, such as spectral ratio or centroid frequency shift. These methods are realized using only observed viscoacoustic records, by quantifying the change of instantaneous amplitude spectra along traveltime. We could also incorporate the preconditioning and regularization shown in equation 11 into these classic Q estimation methods so that they can provide satisfying estimation for deriving Q-reflectivities via piecewise linear regression. The crucial parameter for the piecewise linear regression is the number of Q interfaces. In application, we recommend setting the Q-interface number according to the number of low-Q anomalies one seeks to differentiate along depth. When in doubt, it is recommended to choose a slightly larger number of Q interfaces.

After obtaining reliable virtual Q-reflection events, the image quality, in terms of positioning and resolution, of the Q-interface images strongly correlates with the kinematic accuracy of the migration velocity. Since the virtual Q-reflection estimation is almost decoupled from the velocity analysis, our workflow can provide updated Q-interface images very efficiently when an updated velocity model is obtained.

Finally, we are only considering the acoustic case in this paper, without taking the elastic effects into account. However, the effects of amplitude mismatch between the modeled acoustic waveform and the observed viscoelastic waveform caused by density and S-wave velocity variation could be partially mitigated by the windowed normalization shown in equation 6.

CONCLUSIONS

We proposed an RTM-based Q-interface imaging method, which utilizes virtual Q reflections generated from data-domain estimated attenuated traveltime. Our method essentially derives the Q-interface information as the virtual Q reflectivity by comparing the attenuated traveltime estimated along adjacent near-offset reflection wave-paths. The derivation of the virtual Q reflectivity is achieved via two data-domain inversion processes: match-filter-based waveform inversion for estimating the attenuated traveltime, and piecewise linear regression for accurate and stable calculation of the virtual Q reflectivity. Synthetic examples have demonstrated that the Q-interface imaging method provides a high-resolution illustration for the top and bottom boundaries of the typical isolated low-Q anomaly with proper positioning and interpretable polarity. Moreover, the piecewise linear regression also helps to infer the Q interfaces that are not co-located with any velocity interfaces, making it suitable for more realistic scenarios.

ACKNOWLEDGEMENT

The authors would like to thank for the financial support from the EDB Petroleum Engineering Professorship. We thank the editor in chief Jeffrey Shragge, the assistant editor Dr. Colin Farquharson, the associate editor Tristan van Leeuwen, and three anonymous reviewers for their constructive comments and suggestions, which have greatly aided us in improving the quality of the paper.

APPENDIX A

FORWARD Q FILTERING

According to the Constant Q theory (Kjartansson, 1979), the complex phase velocity for viscoacoustic wave propagation in a heterogeneous Q media is

$$c_v(\mathbf{x}) = c_0(\mathbf{x})\cos(\pi\gamma(\mathbf{x})/2)(i\omega/\omega_0)^{\gamma(\mathbf{x})}, \tag{A-1}$$

with $\mathbf{x}$ the spatial position in the model domain, i the imaginary unit, ω the angular frequency, $c_0(\mathbf{x})$ the velocity model for a given reference angular frequency ω_0, and $\gamma(\mathbf{x})$

the attenuation model with the following form:

$$\gamma(\mathbf{x}) = \arctan(1/Q(\mathbf{x}))/\pi \approx Q^{-1}(\mathbf{x})/\pi, \tag{A-2}$$

where $Q(\mathbf{x})$ is the heterogeneous Q model.

By comparing $c_v(\mathbf{x})$ with $c_0(\mathbf{x})$, we can obtain a complex phase shift of the viscoacoustic wave with respect to the acoustic wave propagating along any given wave-path:

$$\begin{aligned}\phi &= \int_{\mathbf{\Gamma}} (c_v(\mathbf{x}) - c_0(\mathbf{x}))k(\mathbf{x})dt(\mathbf{x}) \\ &= \int_{\mathbf{\Gamma}} [\cos(\pi\gamma(\mathbf{x})/2)(i\omega/\omega_0)^{\gamma(\mathbf{x})} - 1]\omega dt(\mathbf{x}),\end{aligned} \tag{A-3}$$

where ϕ is the complex phase shift corresponding to the given wave-path $\mathbf{\Gamma}$, $dt(\mathbf{x})$ denotes the discrete acoustic traveltime, and $k(\mathbf{x}) = \omega/c_0(\mathbf{x})$ denotes the acoustic wavenumber. The real and imaginary parts of ϕ correspond to velocity dispersion and amplitude decay, respectively.

Due to $\gamma(\mathbf{x})$ ranging between 0 and 1/2, we can approximate equation A-3 by its first-order Taylor expansion at $\gamma(\mathbf{x}) = 0$ as follows:

$$\begin{aligned}\phi &\approx \omega\ln(i\omega/\omega_0)\int_{\mathbf{\Gamma}} \gamma(\mathbf{x})dt(\mathbf{x}) \\ &= \omega\ln(i\omega/\omega_0)\int_0^t \gamma(\tau)d\tau,\end{aligned} \tag{A-4}$$

with $\gamma(\tau)$ the γ value at any given moment τ along $\mathbf{\Gamma}$, and t the total acoustic traveltime along $\mathbf{\Gamma}$.

By substituting equation 1 and A-2 into equation A-4, we have

$$\phi \approx \omega\ln(i\omega/\omega_0)\Psi(t)/\pi. \tag{A-5}$$

Then we can apply the non-stationary filter $\exp(i\phi)$ on the acoustic record trace-by-trace to transform it into viscoacoustic record, which provides us the forward Q filtering

$$\begin{aligned} u(x_s,x_r,t) &= \frac{1}{2\pi}\int \tilde{R}(x_s,x_r,\omega)\exp[i(\phi+\omega t)]d\omega \\ &= \frac{1}{2\pi}\int \tilde{R}(x_s,x_r,\omega)\exp[i\omega(\ln(i\omega/\omega_0)\Psi(x_s,x_r,t)+t)]d\omega, \end{aligned} \tag{A-6}$$

in which,

$$\tilde{R}(x_s,x_r,\omega) = \int R(x_s,x_r,t)\exp(-i\omega t)dt. \tag{A-7}$$

where $u(x_s,x_r,t)$ is the filtered acoustic record given $\Psi(x_s,x_r,t)$, as x_s, x_r, and t representing source locations, receiver locations and the traveltime, respectively; $R(x_s,x_r,t)$ and $\tilde{R}(x_s,x_r,\omega)$ are acoustic records in time domain and frequency domain, respectively.

According to equation A-7, the first-order derivative of the forward Q filtering operator with respect to the attenuated traveltime $\Psi(x_s,x_r,t)$ is

$$\frac{\partial u(x_s,x_r,t)}{\partial \Psi(x_s,x_r,t)} = \frac{1}{2\pi}\int \tilde{R}(x_s,x_r,\omega)\exp[i\omega(\ln(i\omega/\omega_0)\Psi(x_s,x_r,t)+t)]i\omega\ln(i\omega/\omega_0)d\omega. \tag{A-8}$$

Both equations A-7 and A-8 require trace-by-trace non-stationary filtering. We achieve them by direct integration in the frequency domain for each trace, whose runtime is shorter than 1 ms for each trace without any parallelization.

APPENDIX B

PRECONDITIONING SMOOTHERS

The preconditioning smoother G used for $\Psi_{s,r,t}$ inversion is defined in (x_s,x_r,t) domain. For a simple implementation, we apply three 1-D smoothers sequentially. The first 1-D smoother is designed along travel time for each trace. The second and third 1-D smoothers are defined across adjacent traces in the common shot gather and common offset gather respectively. For the attenuated traveltime along t, we expect some first-order discontinuity due to its piecewise linear property. Therefore, we use the following smoother:

$$y = \exp(|x|/(bl)), \tag{B-1}$$

where y is the filter coefficients, x ranges from $-l$ to l, where l is the half length of the smoother, and b ranging from 0 to 1 is the parameter to control the smoothness of the filter: larger b provides flatter filter. This filter mimics the shape of inverse Laplacian operator so that it could possess the edge-preserving power to some extent. As for horizontal smoothers, we use the same type of smoother shown in equation B-1 along x_s in the common offset gather, whereas we use Gaussian smoother along x_r in the common shot gather as follows:

$$y = \exp(-\frac{x^2}{2(\sigma l)^2}), \tag{B-2}$$

where σ ranging from 0 to 1 is the parameter controlling the smoothness of the filter: larger σ provides flatter filter. The Gaussian filter shown in equation B-2 in comparison with the filter shown in equation B-1 generally provides more smoothing power. We use this Gaussian filter because the accumulative attenuation at the same traveltime across adjacent traces corresponding to the same shot location (in common shot gather) should be more similar than those corresponding to different shot locations (for common offset gather), especially when the offset range is relatively small.

As for the preconditioning smoother H used in $\mathbf{T}_{s,r}$ and $\mathbf{B}_{s,r}$ inversion which is defined in (x_s, x_r) domain, we simply use the same horizontal 1-D smoothers along x_r in the common shot gather and along x_s in the common offset gather, as those used in the $\Psi_{s,r,t}$ estimation.

Figure B-1 shows the total six 1-D smoothers utilized for the match-filter-based waveform inversion in the two synthetic examples. The corresponding parameters are also provided.

REFERENCES

Brzostowski, M. A., and G. A. McMechan, 1992, 3D tomographic imaging of near-surface seismic velocity and attenuation: Geophysics, **57**, 396–403.

Carcione, J. M., D. Kosloff, and R. Kosloff, 1988, Wave propagation simulation in a linear viscoacoustic medium: Geophysical Journal International, **93**, 393–401.

Cavalca, M., I. Moore, L. Zhang, S. L. Ng, R. Fletcher, and M. Bayly, 2011, Ray-based tomography for Q estimation and Q compensation in complex media: 81st Annual Conference and Exhibition, SEG, Extended Abstracts, 3989–3993.

Cheng, P., and G. F. Margrave, 2012, Q estimation by a match-filter method: 82th Annual Conference and Exhibition, SEG, Extended Abastrcts, 1–5.

Claerbout, J. F., 1971, Toward a unified theory of reflector mapping: Geophysics, **36**, 467–481.

Dutta, G., and G. T. Schuster, 2014, Attenuation compensation for least-squares reverse time migration using the viscoacoustic-wave equation: Geophysics, **79**, no. 6, S251–S262.

———, 2016, Wave-equation Q tomography: Geophysics, **81**, no. 6, R471–R484.

Fletcher, R. P., D. Nichols, and M. Cavalca, 2012, Wavepath-consistent effective Q estimation for Q-compensated reverse-time migration: 74th Annual Conference and Exhibition, EAGE, Extended Abastrcts, cp–293.

Fomel, S., L. Ying, and X. Song, 2013, Seismic wave extrapolation using lowrank symbol approximation: Geophysical Prospecting, **61**, 526–536.

French, W. S., 1975, Computer migration of oblique seismic reflection profiles: Geophysics, **40**, 961–980.

Guo, P., and G. A. McMechan, 2018, Compensating Q effects in viscoelastic media by adjoint-based least-squares reverse time migration: Geophysics, **83**, no. 2, S151–S172.

Hu, W., J. Liu, L. Bear, and C. Marcinkovich, 2011, A robust and accurate seismic attenuation tomography algorithm: 81st Annual Conference and Exhibition, SEG, Extended Abstracts, 2727–2731.

Kamei, R., and R. Pratt, 2013, Inversion strategies for visco-acoustic waveform inversion: Geophysical Journal International, **194**, 859–884.

Kjartansson, E., 1979, Constant Q-wave propagation and attenuation: Journal of Geophysical Research: Solid Earth, **84**, 4737–4748.

Lin, R., A. Vesnaver, G. Bohm, and J. M. Carcione, 2018, Broad-band viscoacoustic Q-factor imaging by seismic tomography and instantaneous frequency: Geophysical Journal International, **214**, 672–686.

McMechan, G. A., 1983, Migration by extrapolation of time-dependent boundary values: Geophysical Prospecting, **31**, 413–420.

Müller, T. M., B. Gurevich, and M. Lebedev, 2010, Seismic wave attenuation and dispersion resulting from wave-induced flow in porous rocks — A review: Geophysics, **75**, no. 5, 75A147–75A164.

Qi, Q., T. M. Müller, and M. Pervukhina, 2017, Sonic Q_P/Q_S ratio as diagnostic tool for shale gas saturation: Geophysics, **82**, no. 3, MR97–MR103.

Quan, Y., and M. Harris, 1997, Seismic attenuation tomography using the frequency shift method: Geophysical Prospecting, **62**, 895–905.

Shen, Y., B. Biondi, and R. Clapp, 2018, Q-model building using one-way wave-equation migration Q analysis — Part 1: Theory and synthetic test: Geophysics, **83**, no. 2, S93–S109.

Stoffa, P. L., J. T. Fokkema, R. de Luna Freire, and W. Kessinger, 1990, Split-step Fourier migration: Geophysics, **55**, 410–421.

Stopin, A., R. E. Plessix, H. Kuehl, V. Goh, and K. Overgaag, 2016, Application of Visco-acoustic Full Waveform Inversion for Gas Cloud Imaging and Velocity Model Building: 78th Annual Conference and Exhibition, EAGE, Extended Abastrcts, 1–5.

Sun, J., S. Fomel, and T. Zhu, 2015, Preconditioning least-squares RTM in viscoacoustic media by Q-compensated RTM: 85th Annual Conference and Exhibition, SEG, Extended Abastrcts, 3959–3965.

Toksoz, M. N., D. H. Johnston, and A. Timur, 1979, Attenuation of seismic waves in dry and saturated rocks: I. Laboratory measurements: Geophysics, **44**, 681–690.

Wang, Y., 2002, A stable and efficient approach of inverse Q filtering: Geophysics, **67**, 657–663.

Xue, Z., J. Sun, S. Fomel, and T. Zhu, 2018, Accelerating full-waveform inversion with attenuation compensation: Geophysics, **83**, no. 1, A13–A20.

Zhu, T., J. B. Ajo-Franklin, and T. M. Daley, 2017, Spatiotemporal changes of seismic attenuation caused by injected CO_2 at the Frio-II pilot site, Dayton, TX, USA: Journal of Geophysical Research: Solid Earth, **122**, 7156–7171.

Zhu, T., and J. M. Harris, 2014, Modeling acoustic wave propagation in heterogeneous attenuating media using decoupled fractional Laplacians: Geophysics, **79**, no. 3, T105–T116.

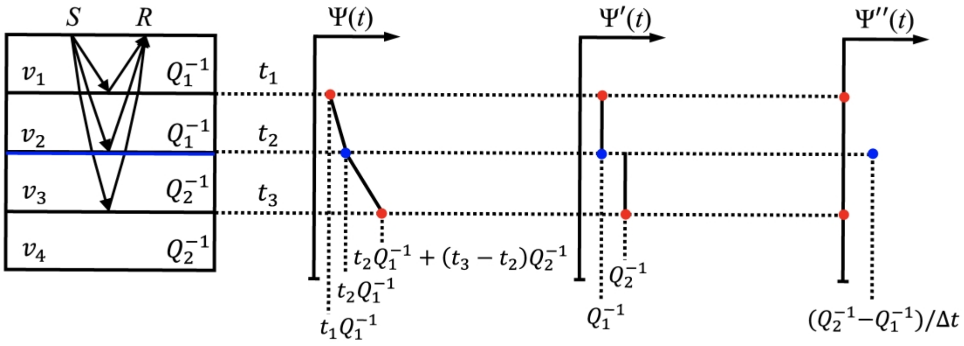

Figure 1. Illustration of the relationship between the attenuated traveltime and the *Q* interface in the reflection regime. *S* and *R* represent source and receiver, respectively. *v* and Q^{-1} with different subscripts denote the velocity and dissipation parameter for different layers. t_1, t_2, and t_3 indicate arrival time of three primary reflections caused by three velocity interfaces, among which a co-located *Q* interface is marked by the blue line.

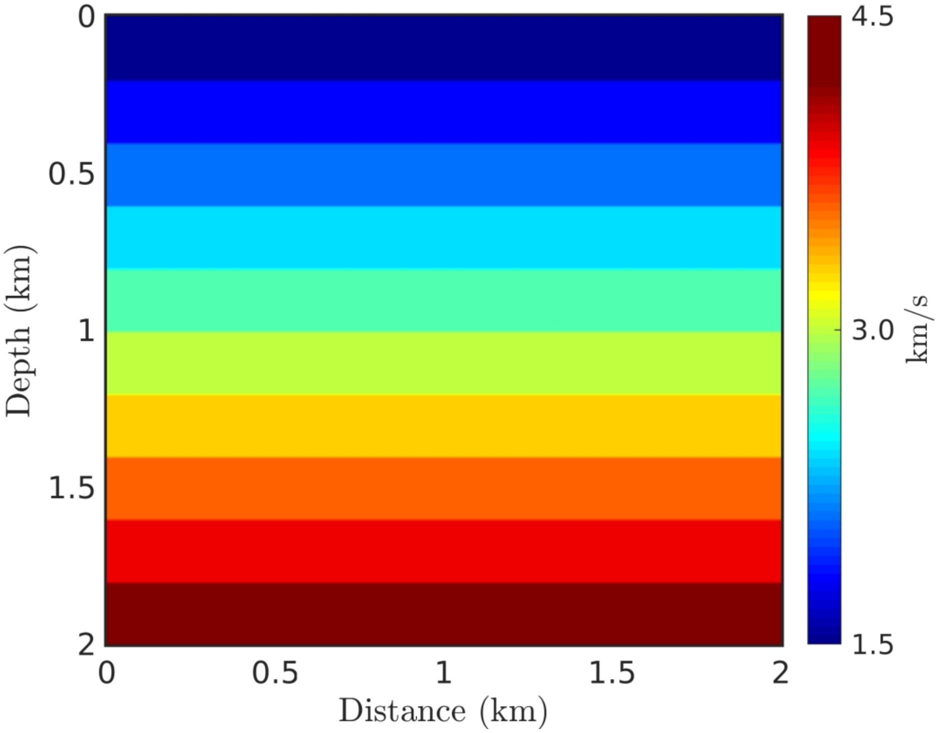

Figure 2a. (a) Simple layered velocity model and (b) its corresponding Q model. Note that the top boundary of the low-Q anomaly is at the depth of 0.5 km, between the second and third velocity interfaces, whereas the bottom boundary is at the depth of 1 km, which is co-located with the fifth velocity interface.

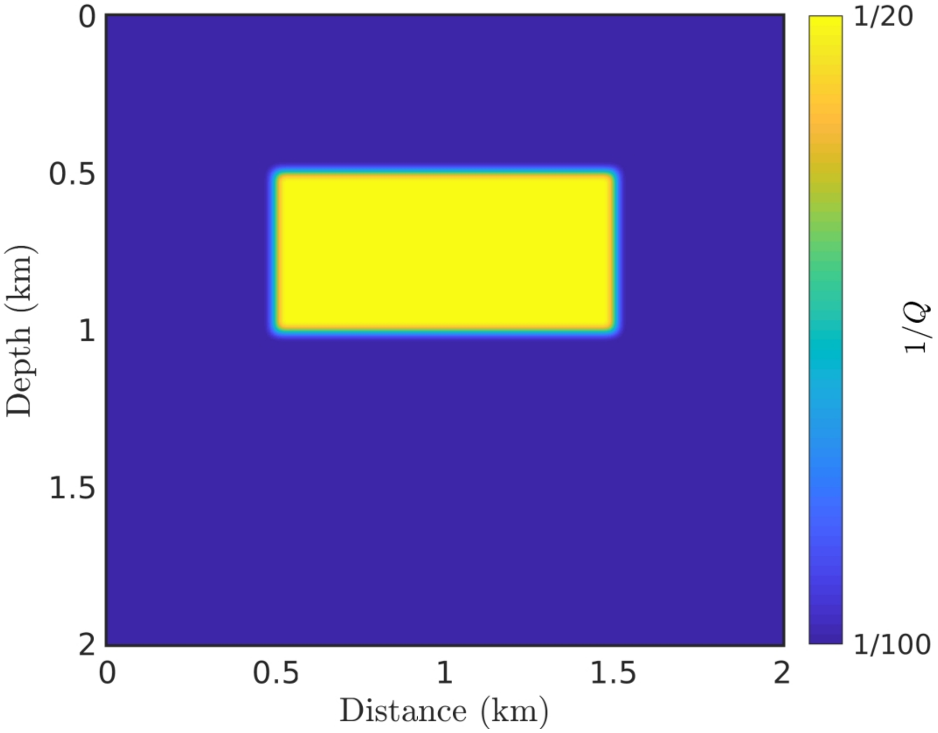

Figure 2b. (a) Simple layered velocity model and (b) its corresponding *Q* model. Note that the top boundary of the low-*Q* anomaly is at the depth of 0.5 km, between the second and third velocity interfaces, whereas the bottom boundary is at the depth of 1 km, which is co-located with the fifth velocity interface.

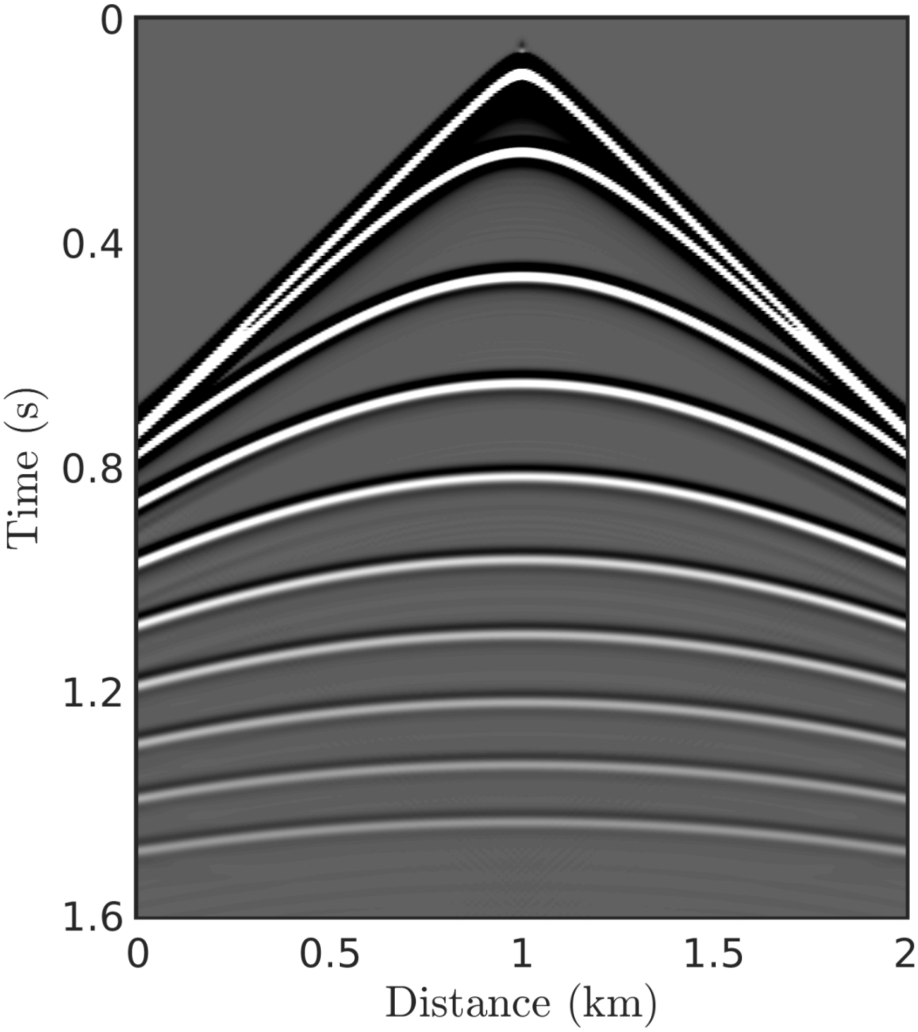

Figure 3a. Synthetic (a) acoustic and (b) viscoacoustic seismograms for the shot gather at x_s = 1000 m.

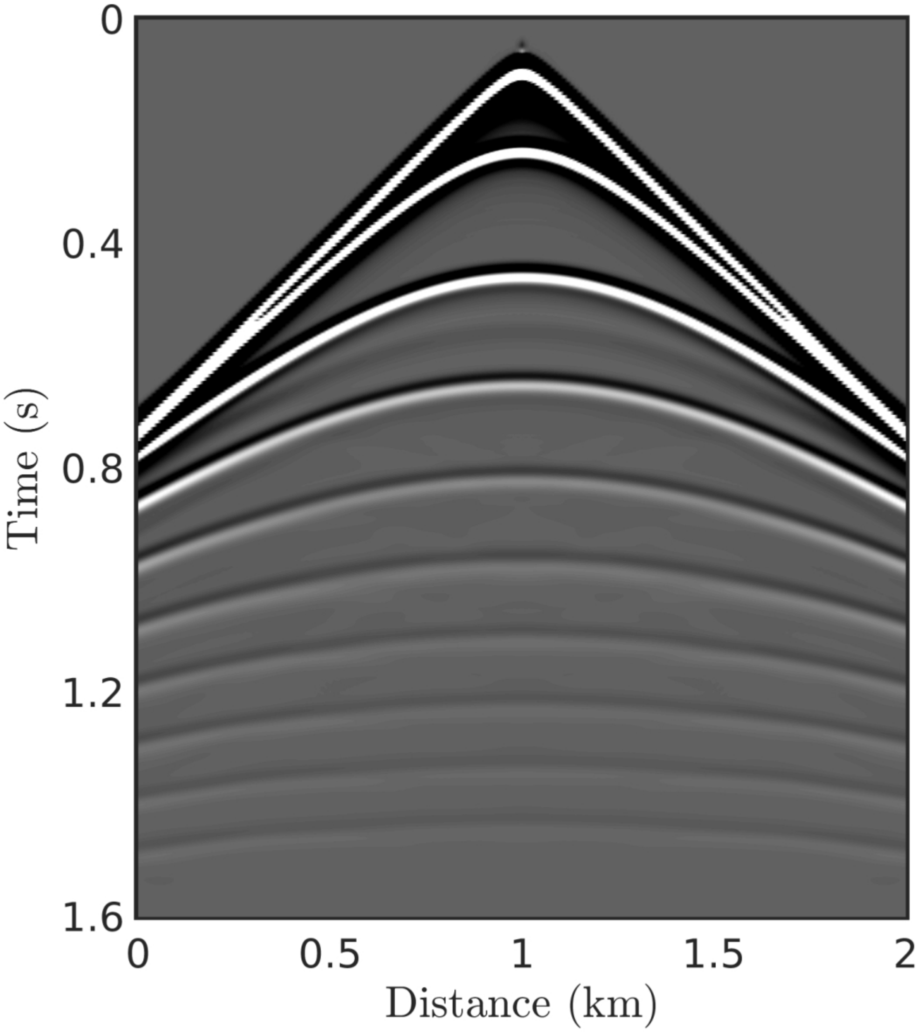

Figure 3b. Synthetic (a) acoustic and (b) viscoacoustic seismograms for the shot gather at x_s = 1000 m.

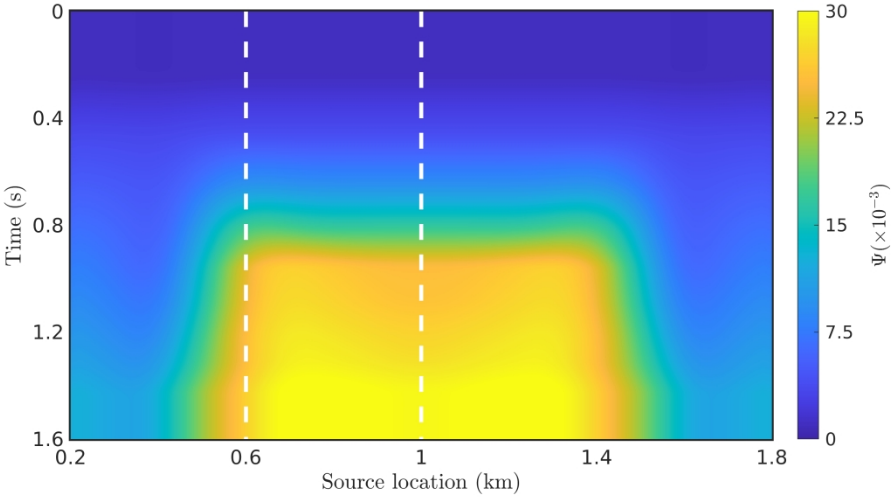

Figure 4a. The attenuated traveltime estimations for (a) the zero-offset gather and two sample common shot gathers at x_s = (b) 600 m and (c) 1000 m. The white dashed lines in (a) indicate source positions of sample shot gathers shown in (b) and (c). The red dashed line in (c) indicates the receiver position (x_r = 1100 m) of the sample trace shown in Figure 5 and 7.

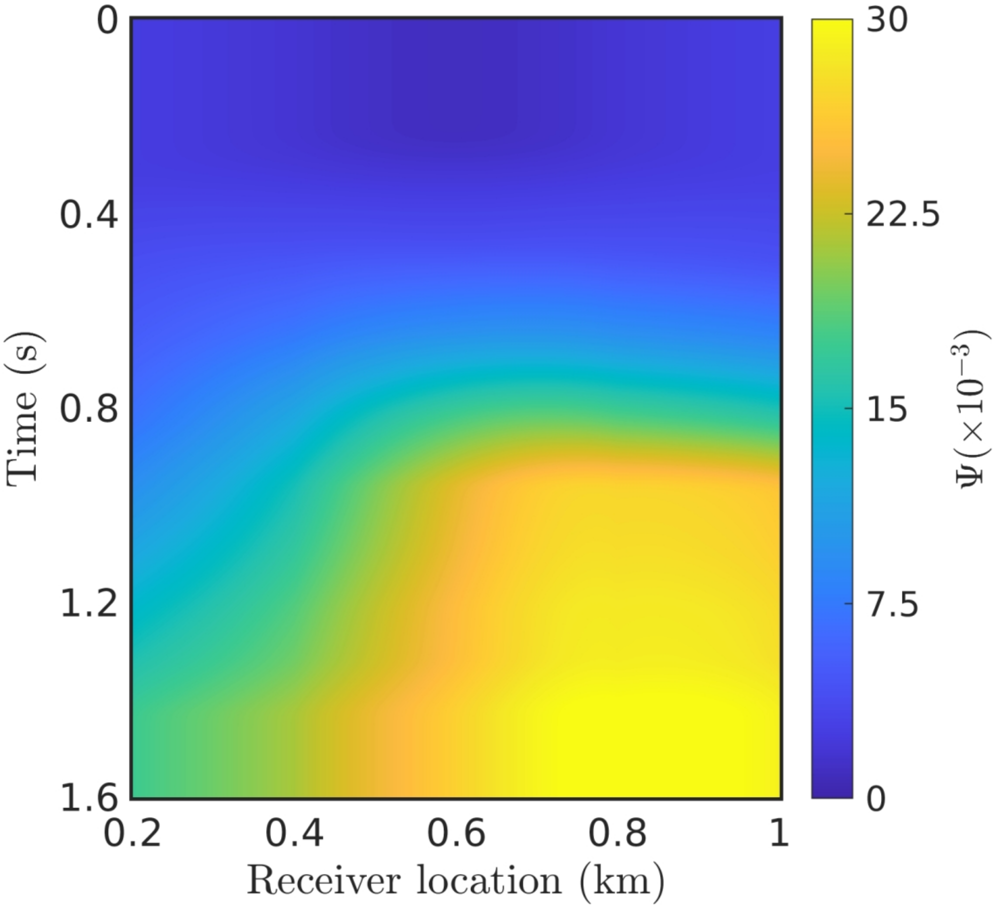

Figure 4b. The attenuated traveltime estimations for (a) the zero-offset gather and two sample common shot gathers at x_s = (b) 600 m and (c) 1000 m. The white dashed lines in (a) indicate source positions of sample shot gathers shown in (b) and (c). The red dashed line in (c) indicates the receiver position (x_r = 1100 m) of the sample trace shown in Figure 5 and 7.

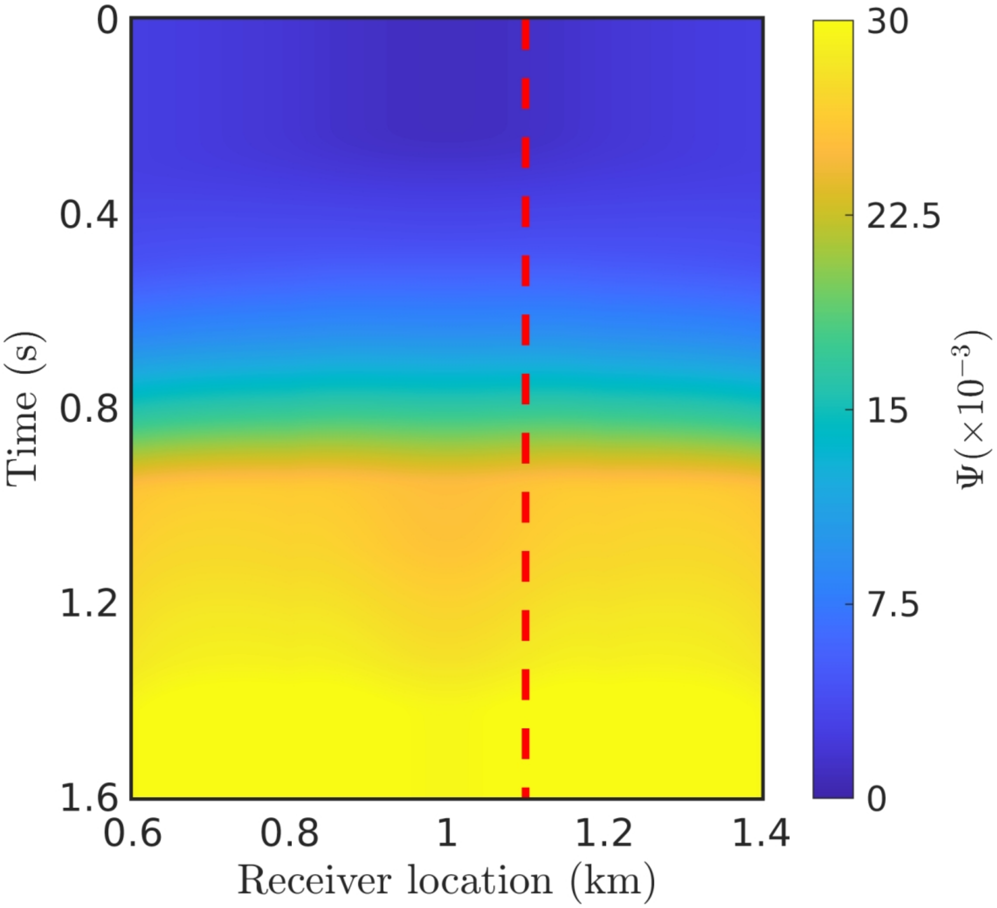

Figure 4c. The attenuated traveltime estimations for (a) the zero-offset gather and two sample common shot gathers at x_s = (b) 600 m and (c) 1000 m. The white dashed lines in (a) indicate source positions of sample shot gathers shown in (b) and (c). The red dashed line in (c) indicates the receiver position (x_r = 1100 m) of the sample trace shown in Figure 5 and 7.

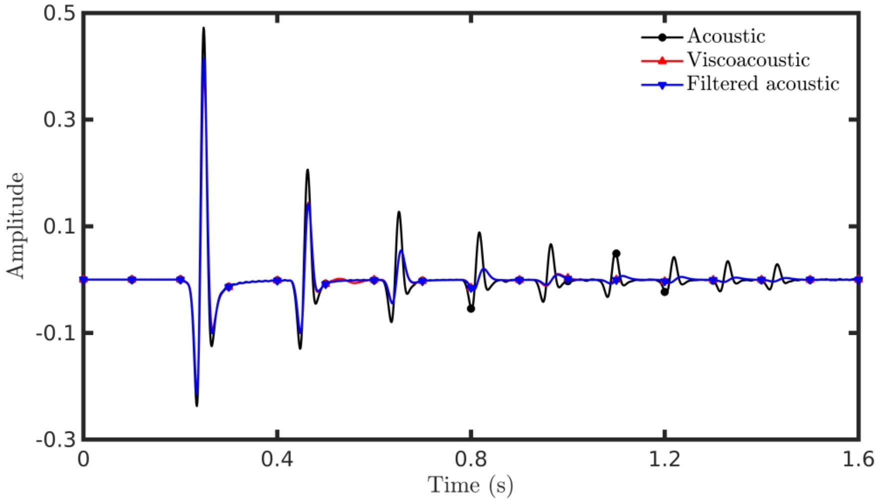

Figure 5. Comparison between the acoustic, the viscoacoustic, and the filtered acoustic waveforms for a sample trace (x_s = 1000 m, x_r = 1100 m) as indicated by the red dashed line in Figure 4c.

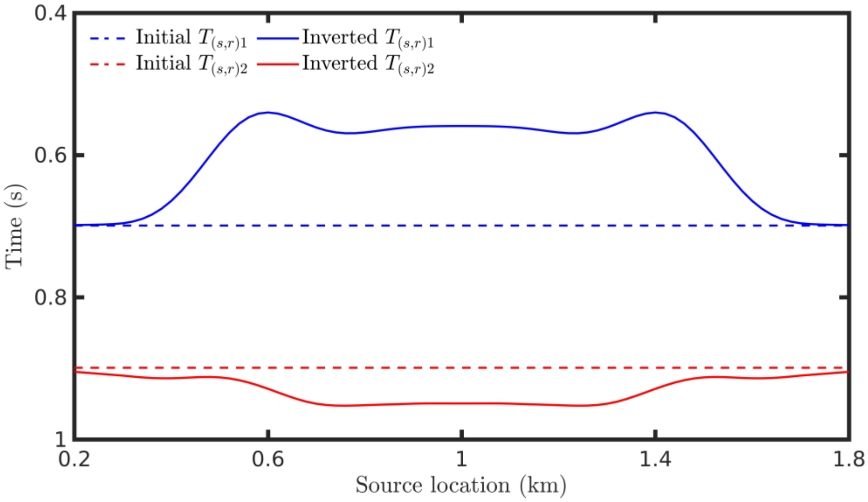

Figure 6a. The initial and inverted (a) turning positions $\boldsymbol{T}_{s,r}$ and (b) slopes $\boldsymbol{B}_{s,r}$ from piecewise linear regression based on the attenuated traveltime estimation shown in Figure 4a. The green dashed lines indicate the horizontal range (560 m, 1440 m) of the low-*Q* anomaly, obtained from 3dB bandwidth of the inverted $\boldsymbol{B}_{(s,r)1}$.

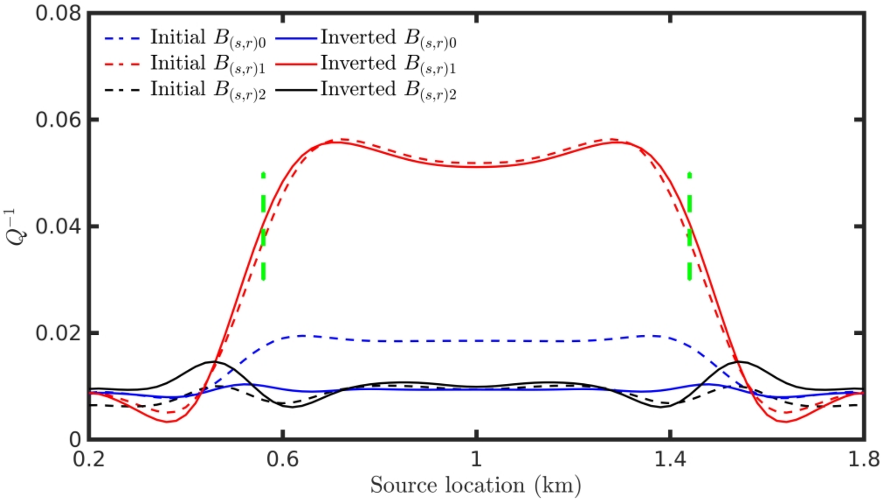

Figure 6b. The initial and inverted (a) turning positions $\boldsymbol{T}_{s,r}$ and (b) slopes $\boldsymbol{B}_{s,r}$ from piecewise linear regression based on the attenuated traveltime estimation shown in Figure 4a. The green dashed lines indicate the horizontal range (560 m, 1440 m) of the low-*Q* anomaly, obtained from 3dB bandwidth of the inverted $\boldsymbol{B}_{(s,r)1}$.

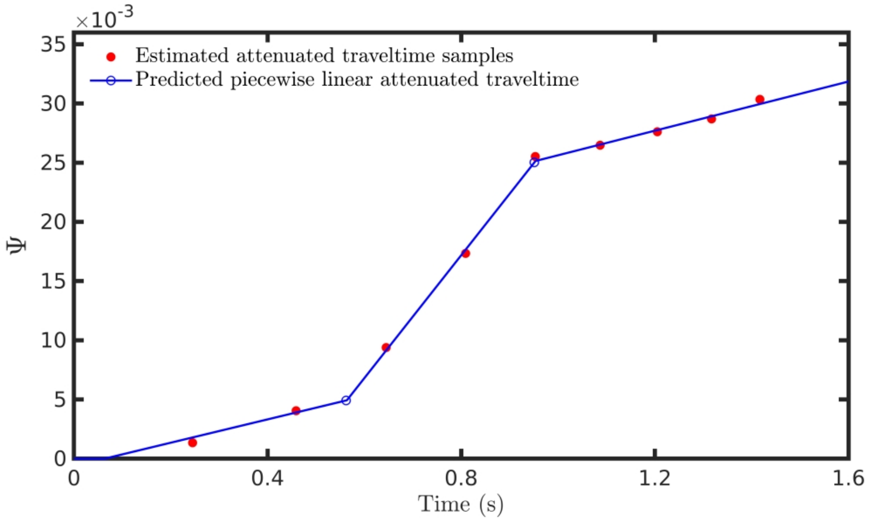

Figure 7. Piecewise linear regression on attenuated traveltime estimation samples $\Psi(x_s = 1000$ m, $x_r = 1100$ m, t s) as indicated by the red dashed line in Figure 4c. The blue circles mark the turning positions, i.e., the Q-interface positions along traveltime.

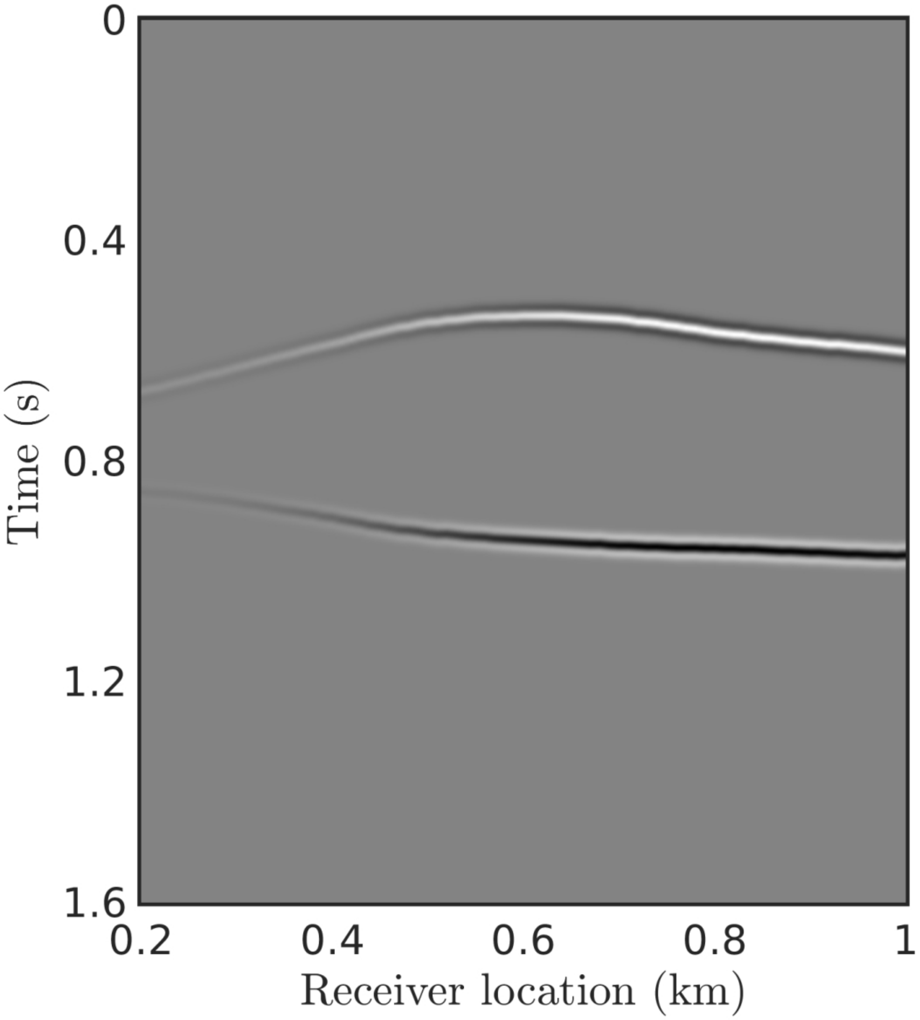

Figure 8a. Generated virtual Q reflection gathers at x_s = (a) 600 m and (b) 1000 m for the attenuated traveltime estimations of common shot gathers shown in Figure 4b and 4c.

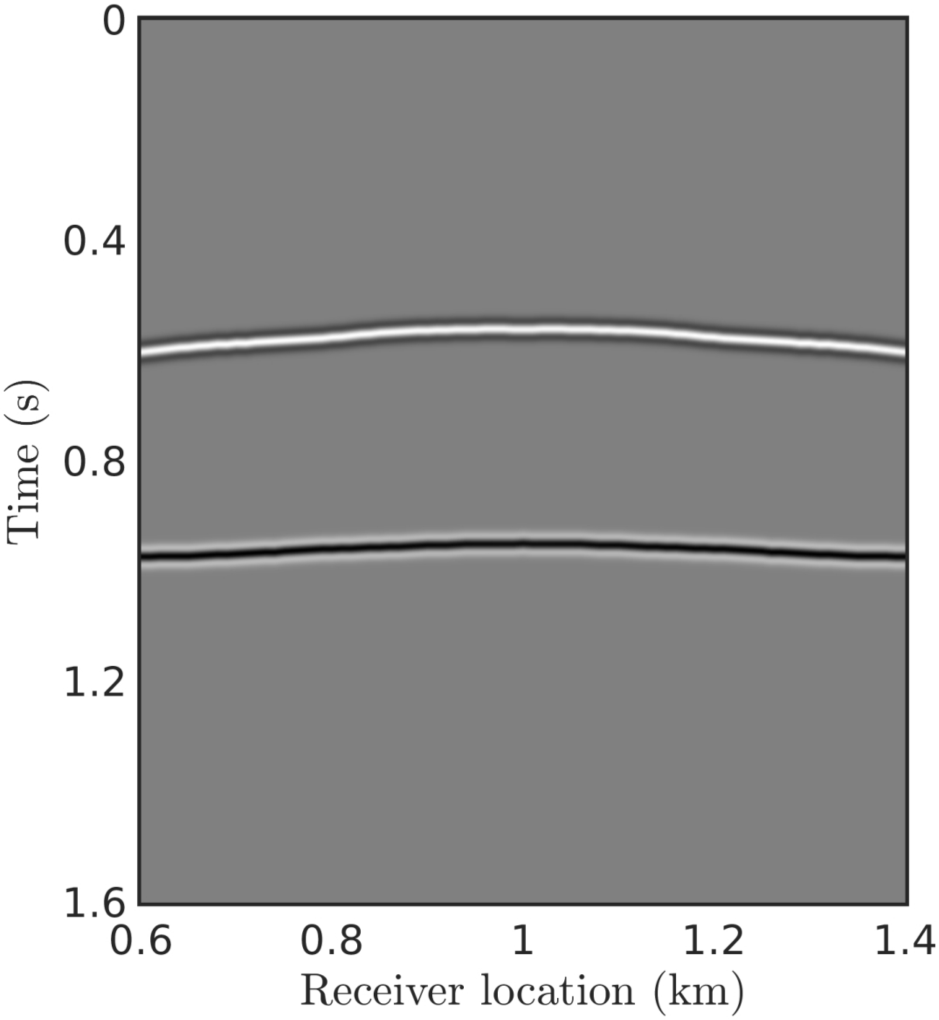

Figure 8b. Generated virtual Q reflection gathers at x_s = (a) 600 m and (b) 1000 m for the attenuated traveltime estimations of common shot gathers shown in Figure 4b and 4c.

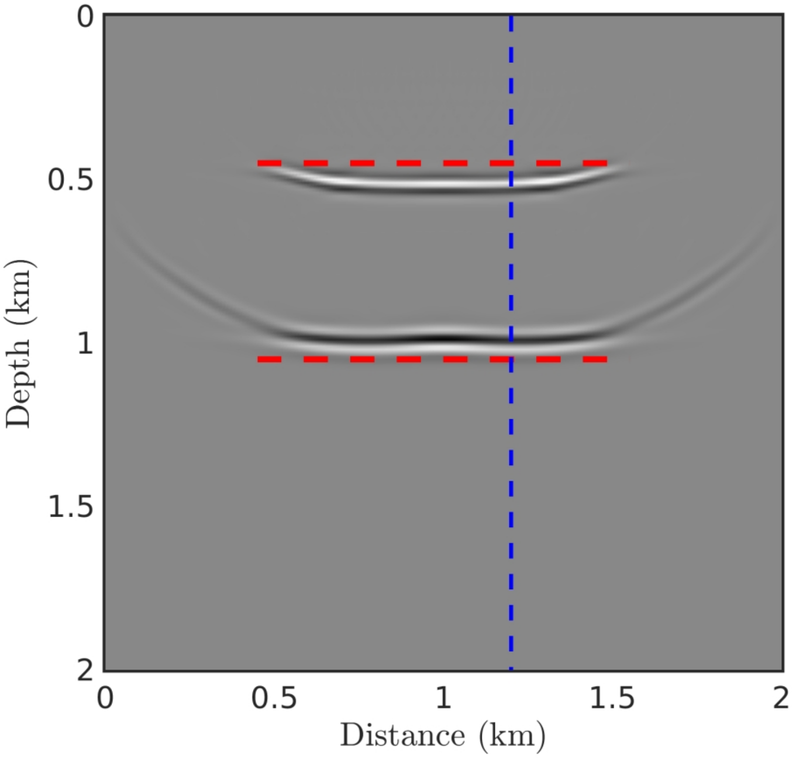

Figure 9a. (a) *Q*-interface image in comparison with (b) the reference *Q* model. The red dashed lines highlight that the imaged top and bottom boundaries are correctly positioned. The blue dashed lines indicate the position of the sample trace shown in Figure 10.

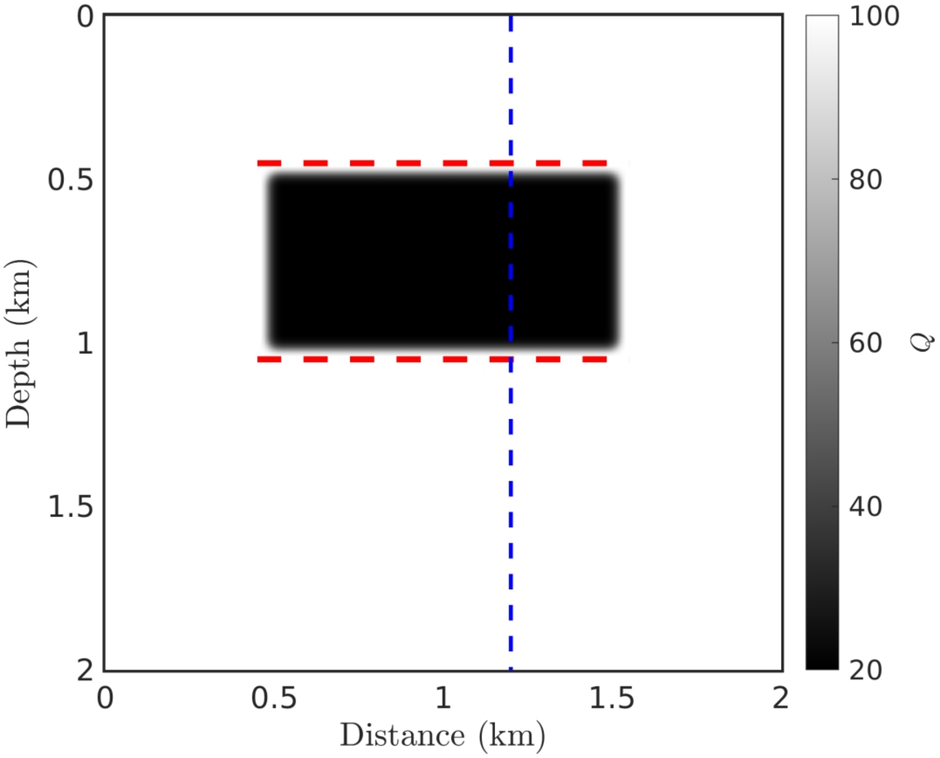

Figure 9b. (a) *Q*-interface image in comparison with (b) the reference *Q* model. The red dashed lines highlight that the imaged top and bottom boundaries are correctly positioned. The blue dashed lines indicate the position of the sample trace shown in Figure 10.

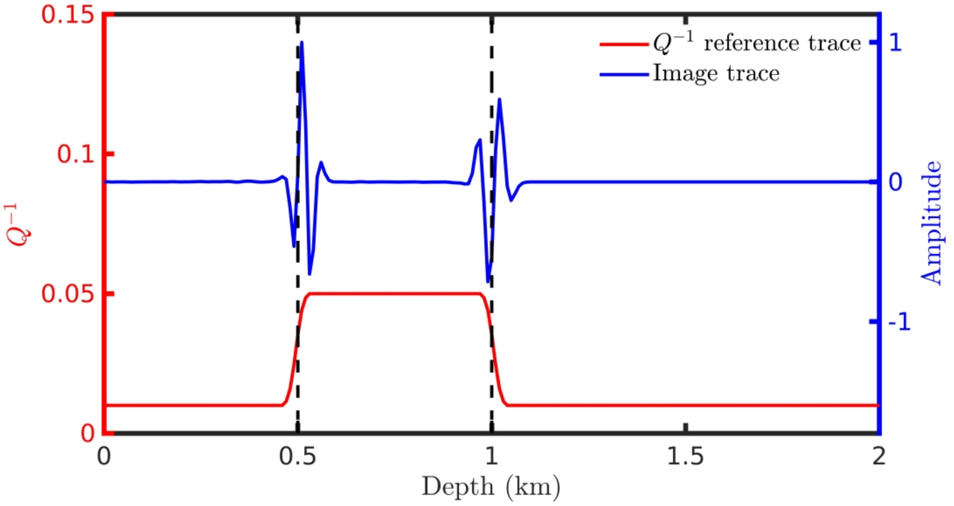

Figure 10. Comparison between *Q* image trace with the reference *Q* model. The distance of the sampled trace is at 1200 m as shown in Figure 9. The black dashed lines indicate the middle positions of the Q^{-1} changes along depth.

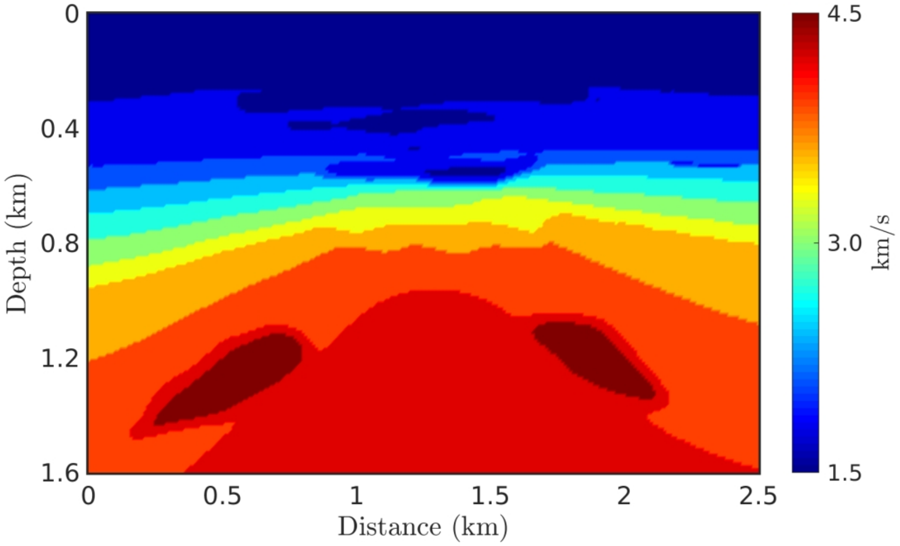

Figure 11a. Gas chimney model: (a) velocity and (b) *Q* models.

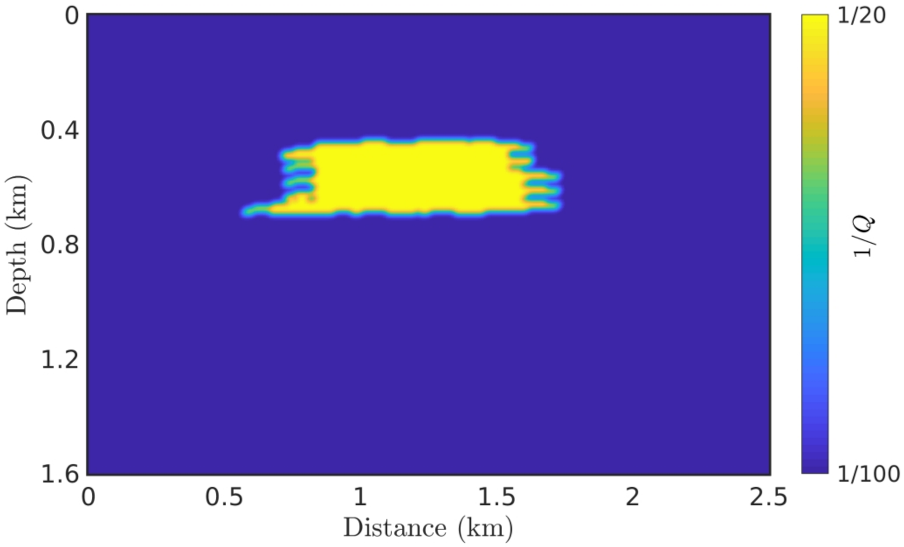

Figure 11b. Gas chimney model: (a) velocity and (b) *Q* models.

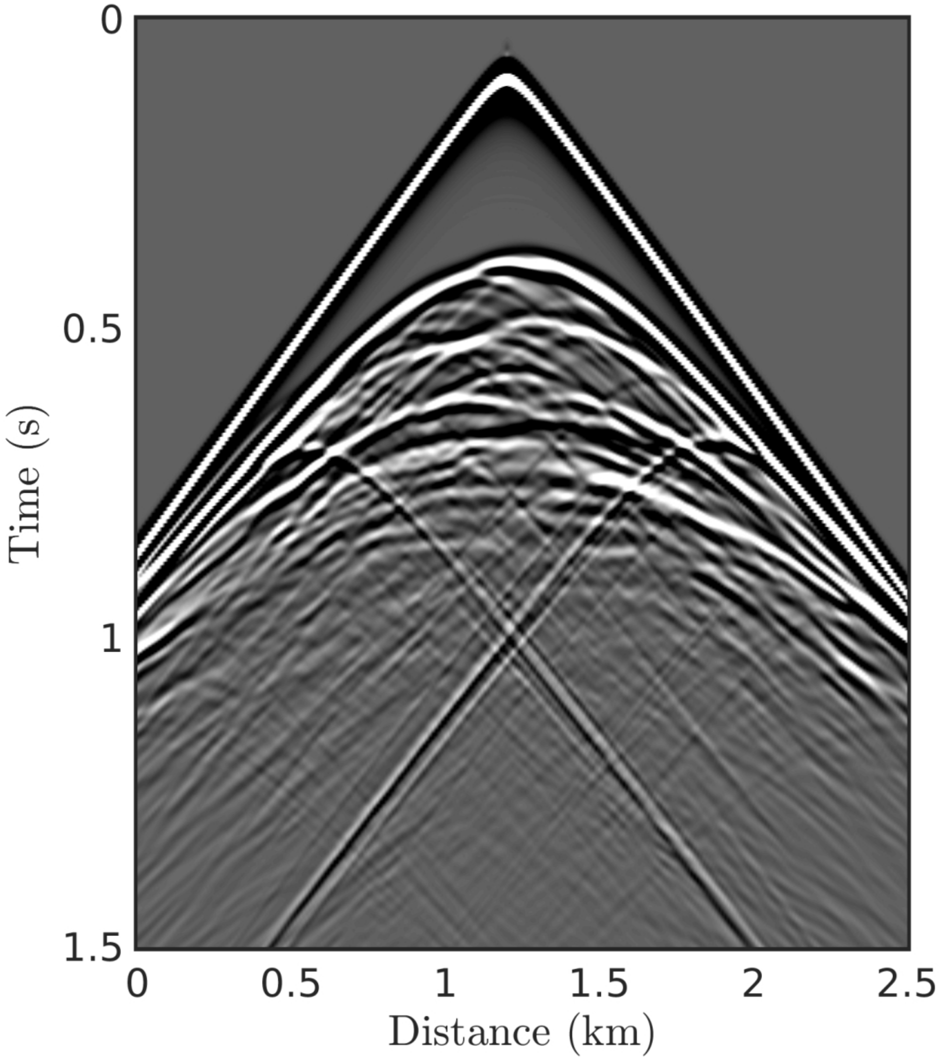

Figure 12a. Synthetic (a) acoustic and (b) viscoacoustic seismograms for the shot gather at x_s = 1200 m.

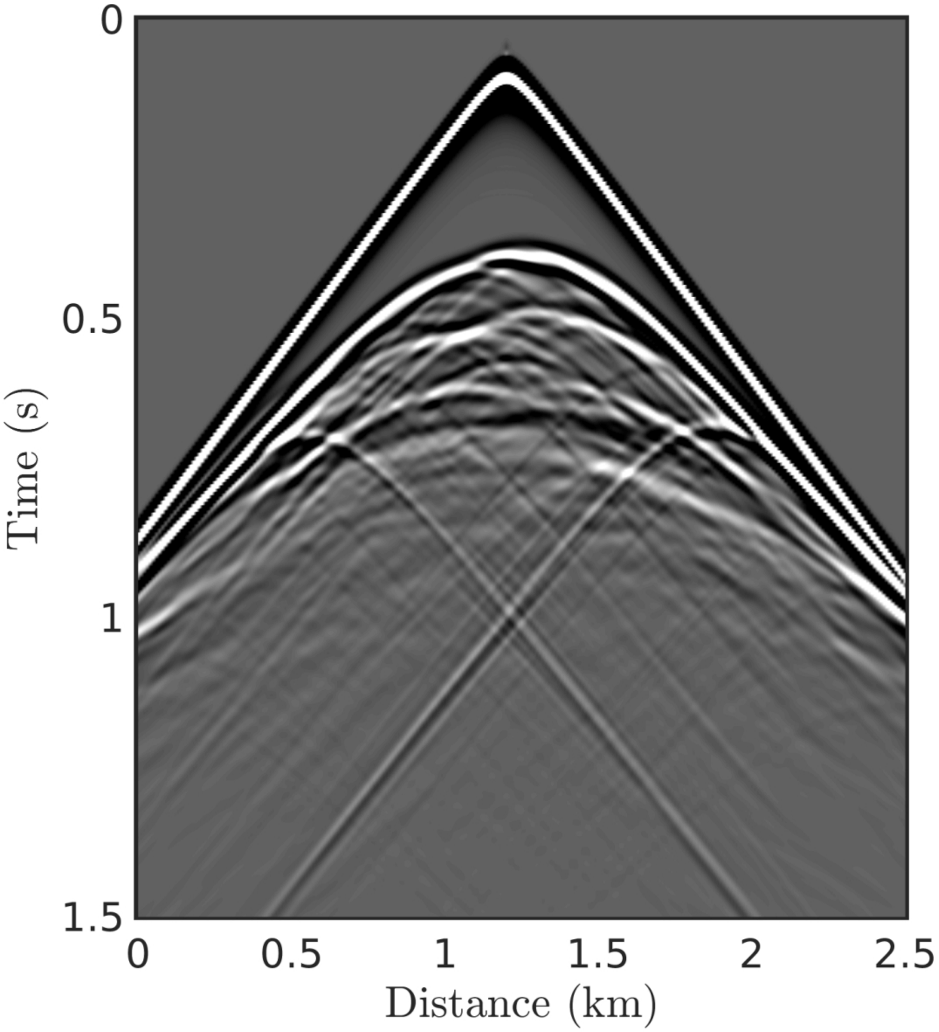

Figure 12b. Synthetic (a) acoustic and (b) viscoacoustic seismograms for the shot gather at x_s = 1200 m.

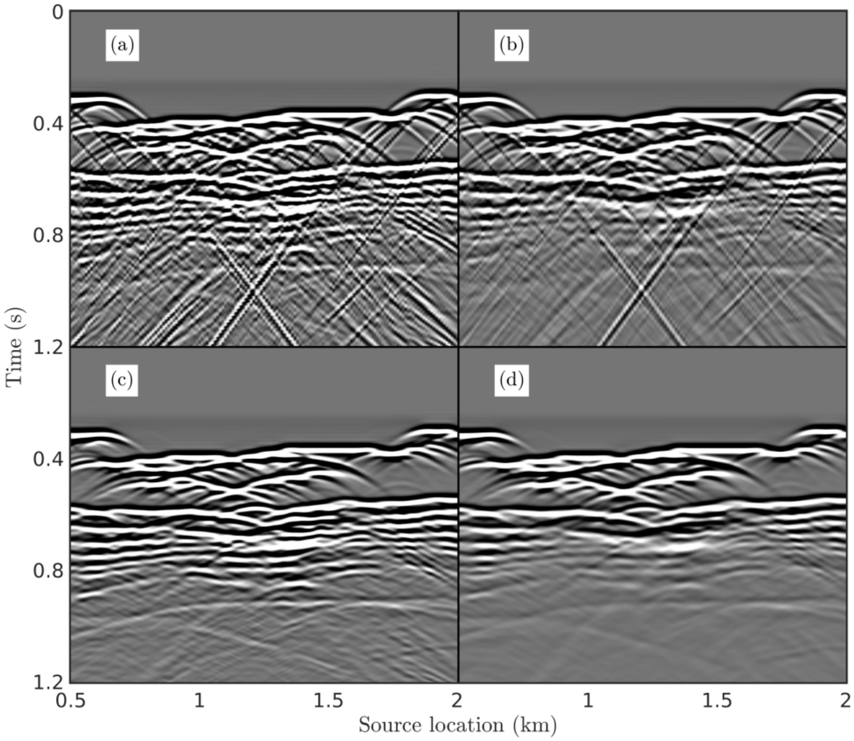

Figure 13. Zero-offset gathers for both acoustic ((a), (c)) and viscoacoustic ((b), (d)) seismograms after muting first arrival. (a) and (b) are before diffraction suppression by f-k filtering; (c) and (d) are after f-k filtering.

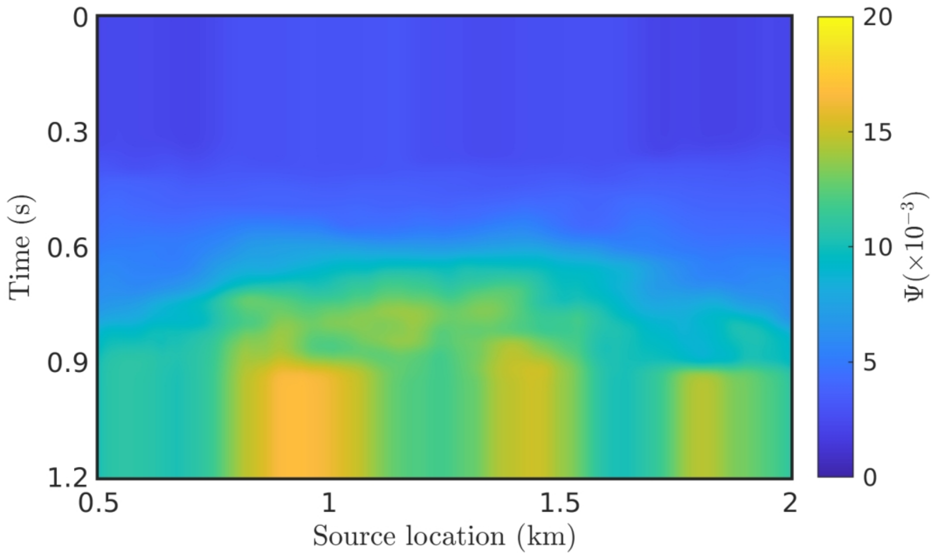

Figure 14a. Zero-offset results for match-filter-based attenuated traveltime estimation ((a) and (c)) and piecewise linear regression ((b) and (d)). (a) and (b) are before diffraction suppression by f-k filtering; (c) and (d) are after f-k filtering. The green dashed lines in (d) indicate the horizontal range (800 m, 1550 m) of the low-*Q* anomaly, obtained from 3dB bandwidth of the inverted $B_{(s,r)1}$ in (d).

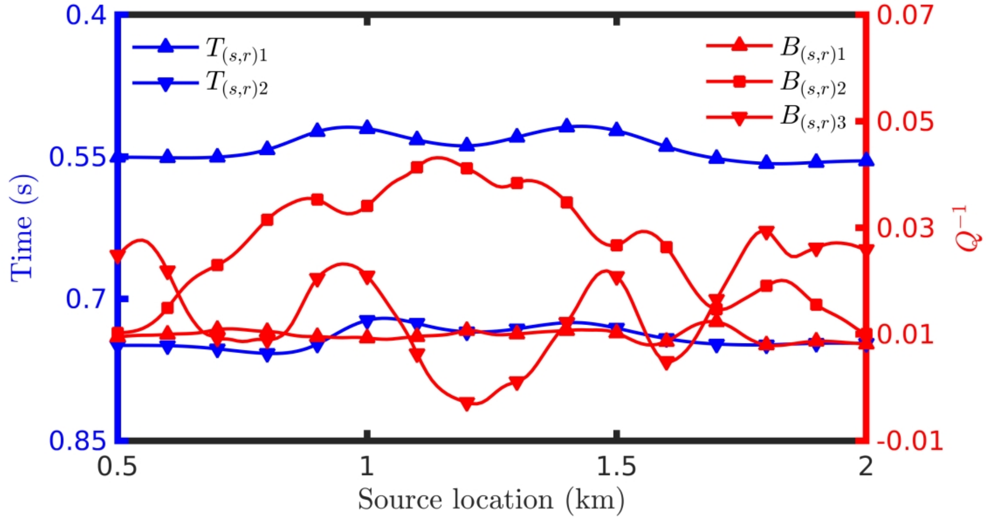

Figure 14b. Zero-offset results for match-filter-based attenuated traveltime estimation ((a) and (c)) and piecewise linear regression ((b) and (d)). (a) and (b) are before diffraction suppression by f-k filtering; (c) and (d) are after f-k filtering. The green dashed lines in (d) indicate the horizontal range (800 m, 1550 m) of the low-*Q* anomaly, obtained from 3dB bandwidth of the inverted $B_{(s,r)1}$ in (d).

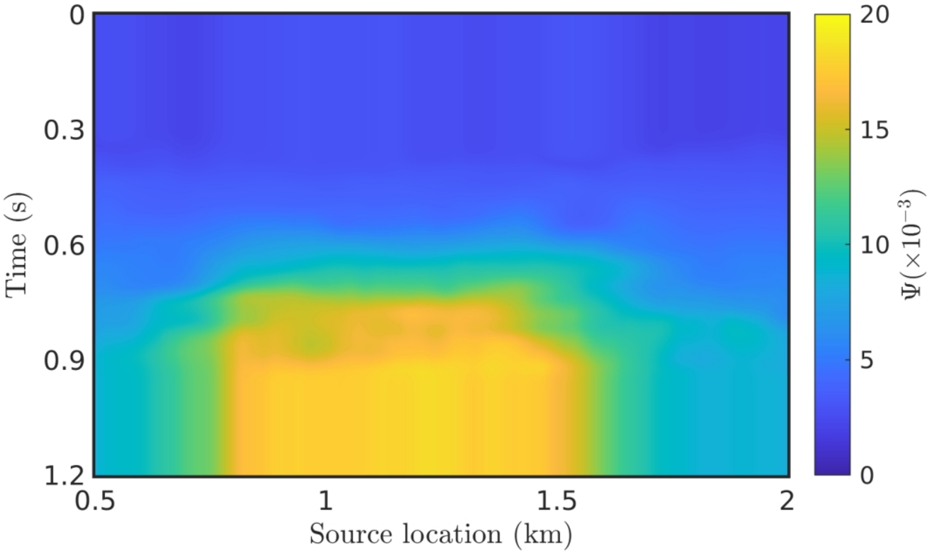

Figure 14c. Zero-offset results for match-filter-based attenuated traveltime estimation ((a) and (c)) and piecewise linear regression ((b) and (d)). (a) and (b) are before diffraction suppression by f-k filtering; (c) and (d) are after f-k filtering. The green dashed lines in (d) indicate the horizontal range (800 m, 1550 m) of the low-*Q* anomaly, obtained from 3dB bandwidth of the inverted $B_{(s,r)1}$ in (d).

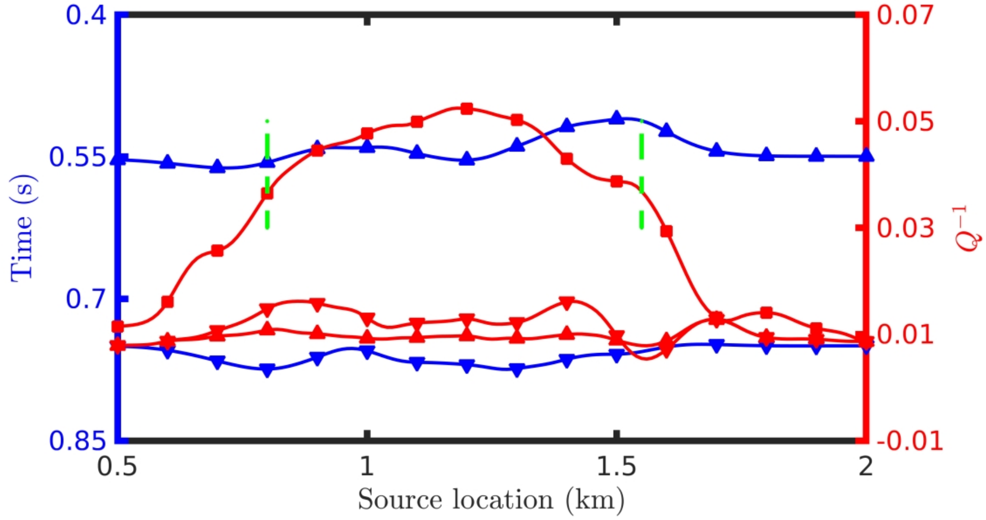

Figure 14d. Zero-offset results for match-filter-based attenuated traveltime estimation ((a) and (c)) and piecewise linear regression ((b) and (d)). (a) and (b) are before diffraction suppression by f-k filtering; (c) and (d) are after f-k filtering. The green dashed lines in (d) indicate the horizontal range (800 m, 1550 m) of the low-*Q* anomaly, obtained from 3dB bandwidth of the inverted $B_{(s,r)1}$ in (d).

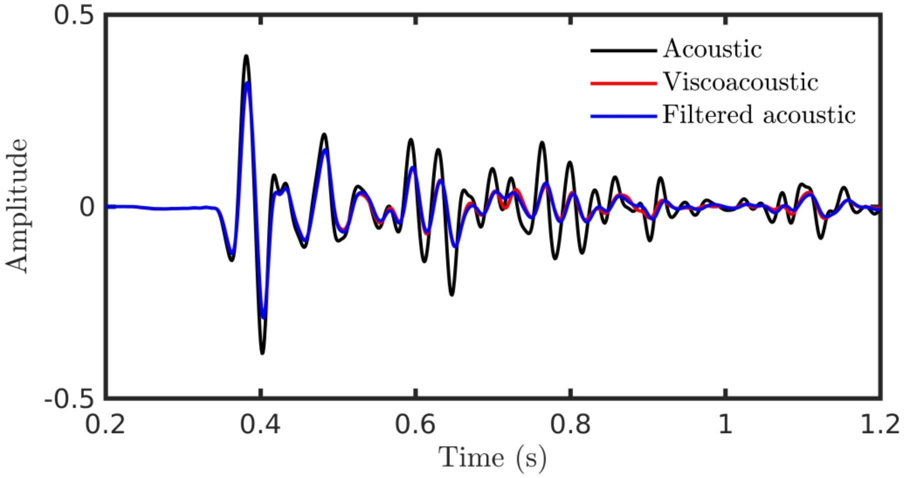

Figure 15a. Sample trace results for match-filter-based attenuated traveltime estimation ((a) and (c)) and piecewise linear regression ((b) and (d)) at x_s = 1300 m, i>x$_r$ = 1300 m. (a) and (b) are obtained from seismograms before diffraction suppression by f-k filtering; (c) and (d) are obtained from seismograms after f-k filtering.

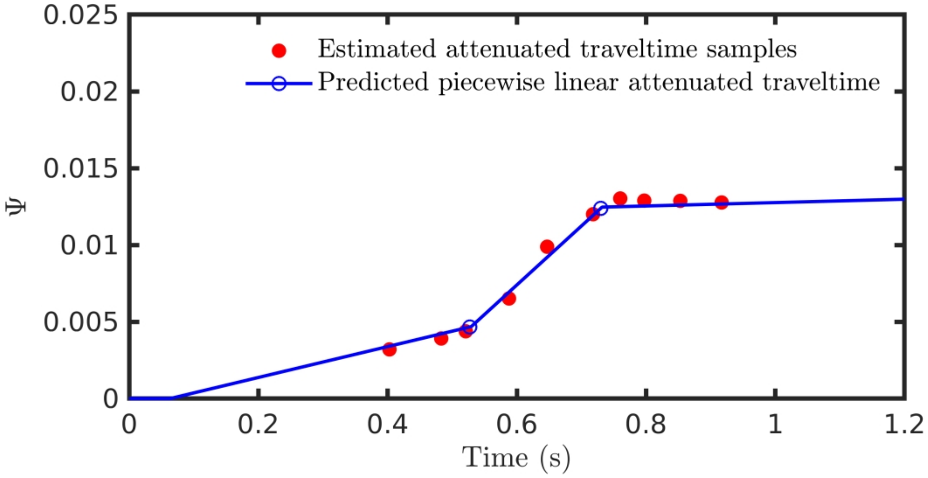

Figure 15b. Sample trace results for match-filter-based attenuated traveltime estimation ((a) and (c)) and piecewise linear regression ((b) and (d)) at x_s = 1300 m, i>x_r = 1300 m. (a) and (b) are obtained from seismograms before diffraction suppression by f-k filtering; (c) and (d) are obtained from seismograms after f-k filtering.

DOI:10.1190/geo2019-0769.1

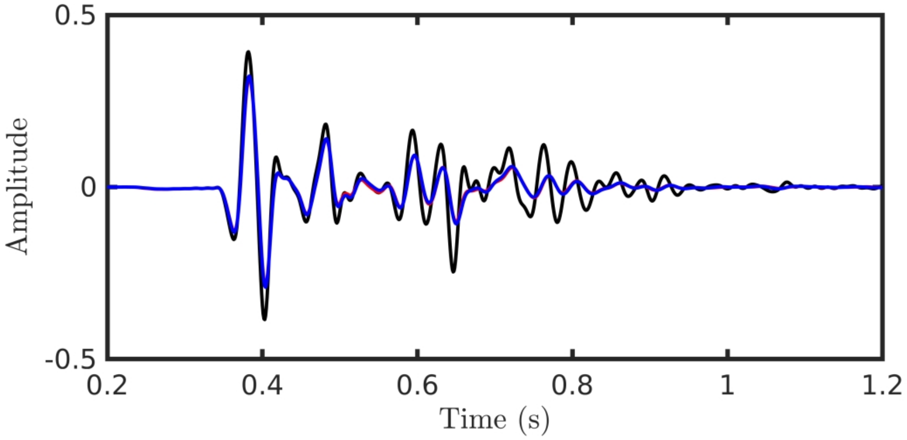

Figure 15c. Sample trace results for match-filter-based attenuated traveltime estimation ((a) and (c)) and piecewise linear regression ((b) and (d)) at x_s = 1300 m, i>x_r = 1300 m. (a) and (b) are obtained from seismograms before diffraction suppression by f-k filtering; (c) and (d) are obtained from seismograms after f-k filtering.

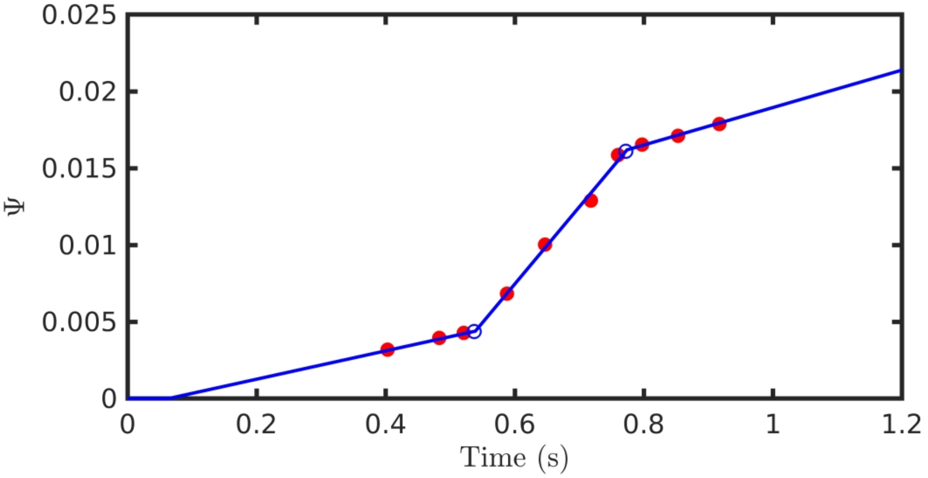

Figure 15d. Sample trace results for match-filter-based attenuated traveltime estimation ((a) and (c)) and piecewise linear regression ((b) and (d)) at x_s = 1300 m, i>x_r = 1300 m. (a) and (b) are obtained from seismograms before diffraction suppression by f-k filtering; (c) and (d) are obtained from seismograms after f-k filtering.

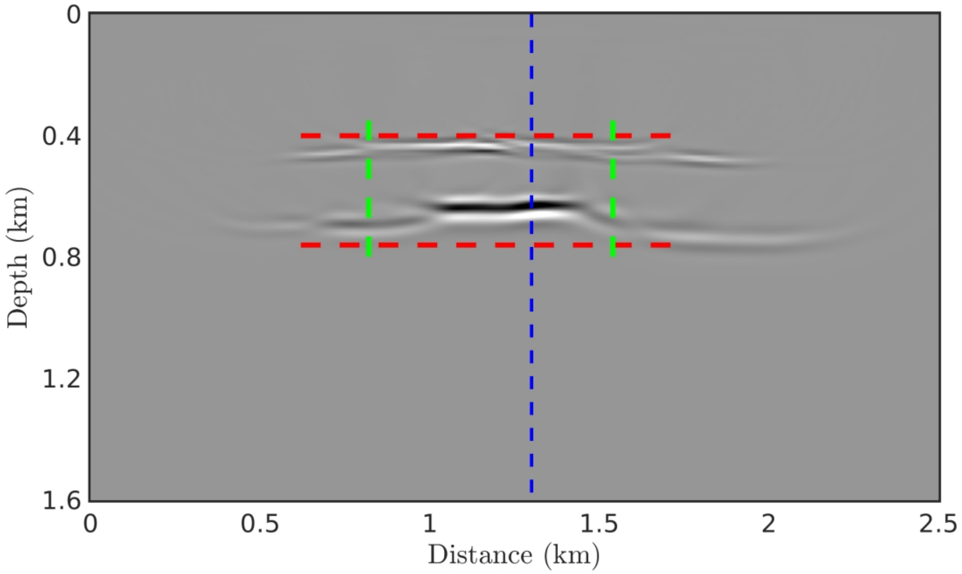

Figure 16a. *Q*-interface images obtained from seismograms (a) before and (b) after f-k filtering, in comparison with (c) the reference *Q* model. The red and green dashed lines approximately mark the vertical and horizontal ranges of the *Q* anomaly. The blue dashed lines indicate the position of the sampled trace shown in Figure 17.

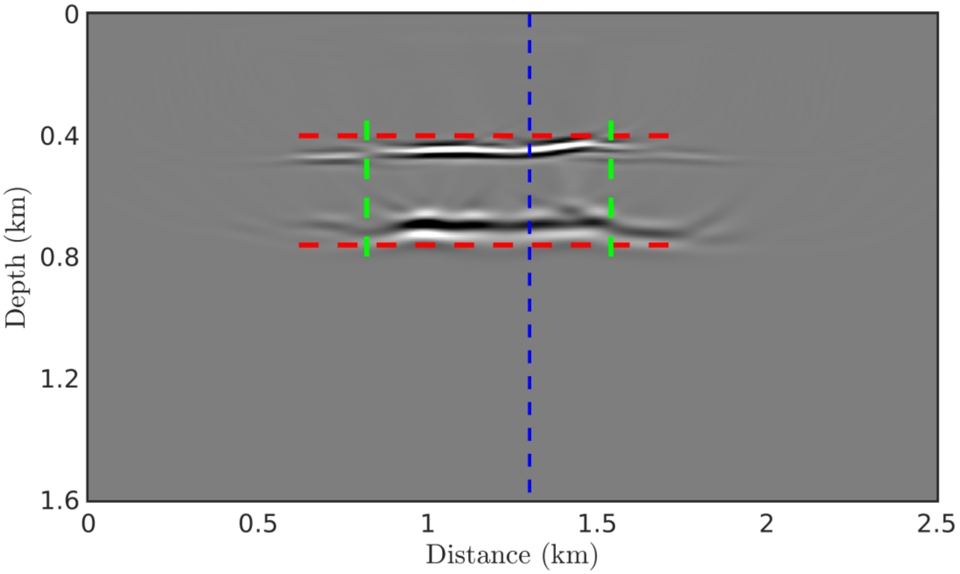

Figure 16b. *Q*-interface images obtained from seismograms (a) before and (b) after f-k filtering, in comparison with (c) the reference *Q* model. The red and green dashed lines approximately mark the vertical and horizontal ranges of the *Q* anomaly. The blue dashed lines indicate the position of the sampled trace shown in Figure 17.

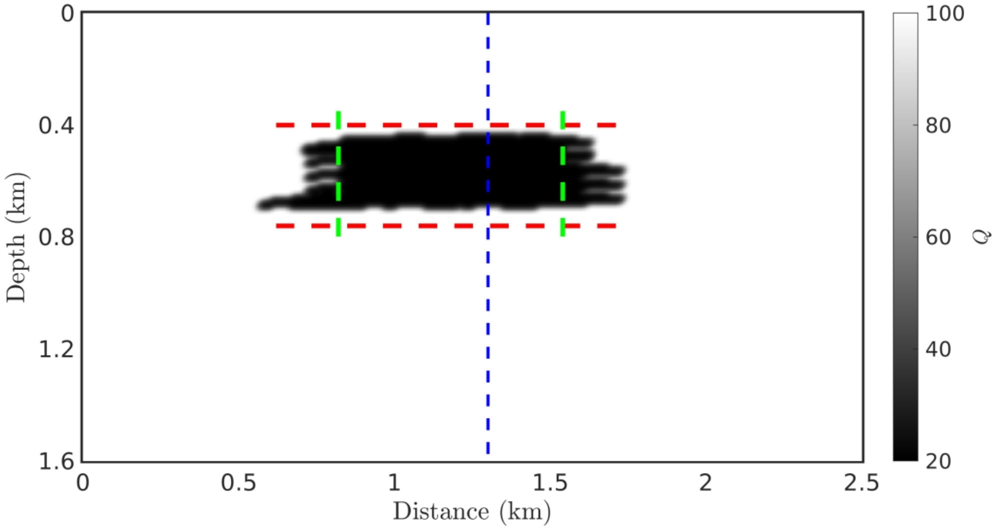

Figure 16c. *Q*-interface images obtained from seismograms (a) before and (b) after f-k filtering, in comparison with (c) the reference *Q* model. The red and green dashed lines approximately mark the vertical and horizontal ranges of the *Q* anomaly. The blue dashed lines indicate the position of the sampled trace shown in Figure 17.

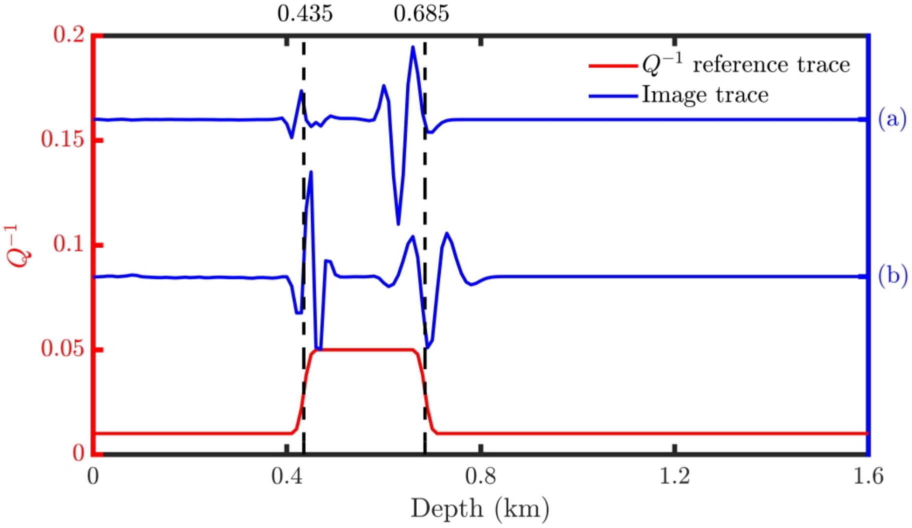

Figure 17. Comparison between *Q*-interface image traces with the reference *Q* model. (a) and (b) represent the image traces sampled from Figure 16a and 16b, respectively. The black dashed lines indicate the middle positions of the Q_{-1} changes along depth.

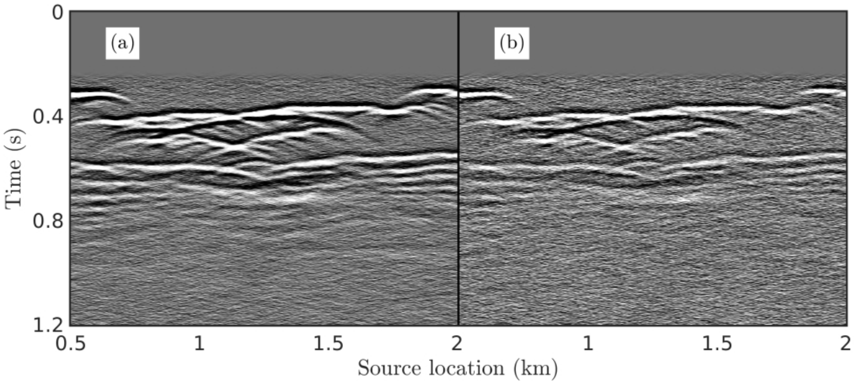

Figure 18. Preprocessed zero-offset gathers of the normalized viscoacoustic data adding different Gaussian random noise with (a) σ_n = 0.005 and (b) 0.01, respectively.

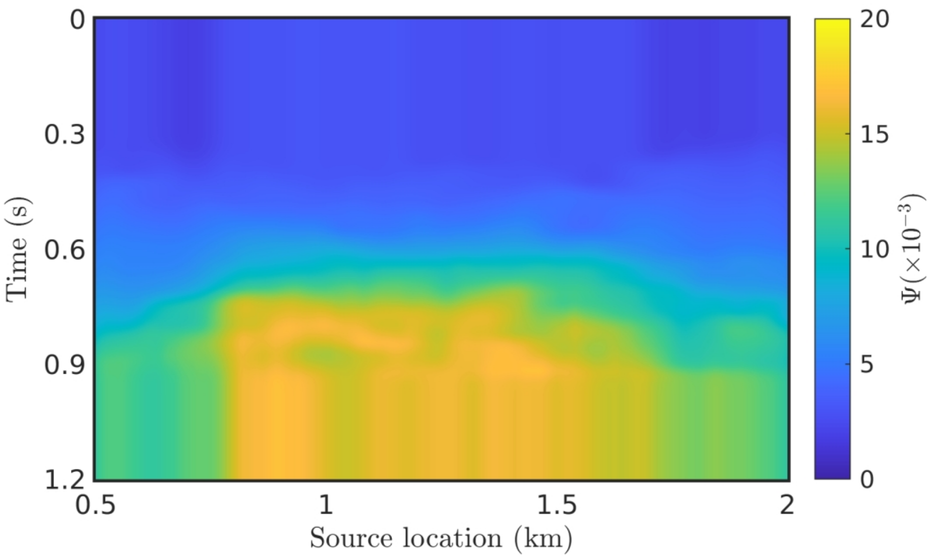

Figure 19a. Zero-offset inversion results for match-filter-based attenuated traveltime estimation ((a), (c)) and piecewise linear regression ((b), (d)). (a) and (b) are obtained from seismograms with Gaussian random noise of σ_n = 0.005; (c) and (d) are obtained from seismograms with Gaussian random noise of σ_n = 0.01.

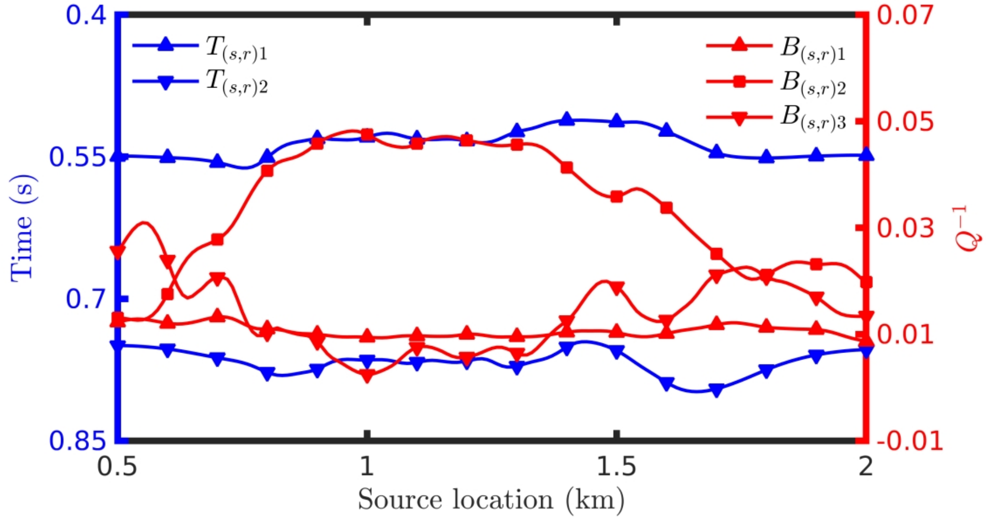

Figure 19b. Zero-offset inversion results for match-filter-based attenuated traveltime estimation ((a), (c)) and piecewise linear regression ((b), (d)). (a) and (b) are obtained from seismograms with Gaussian random noise of σ_n = 0.005; (c) and (d) are obtained from seismograms with Gaussian random noise of σ_n = 0.01.

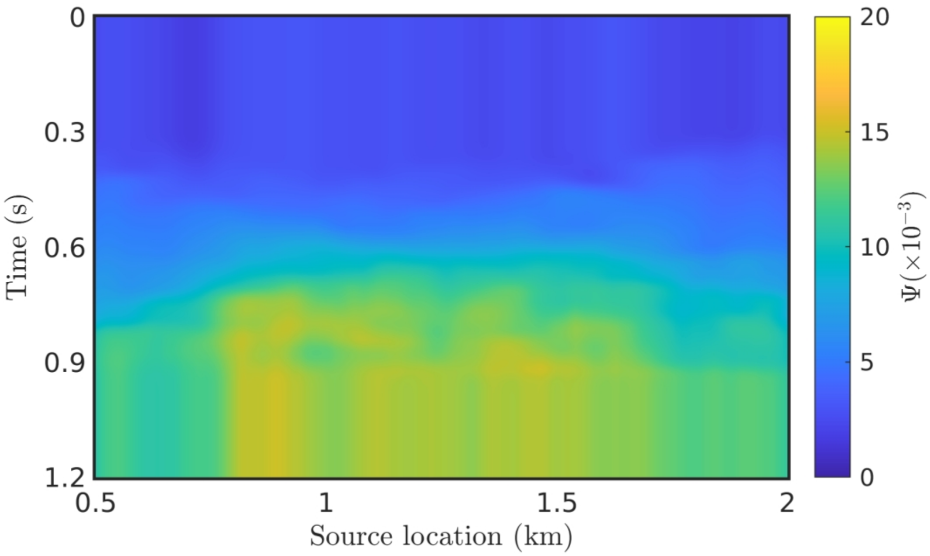

Figure 19c. Zero-offset inversion results for match-filter-based attenuated traveltime estimation ((a), (c)) and piecewise linear regression ((b), (d)). (a) and (b) are obtained from seismograms with Gaussian random noise of σ_n = 0.005; (c) and (d) are obtained from seismograms with Gaussian random noise of σ_n = 0.01.

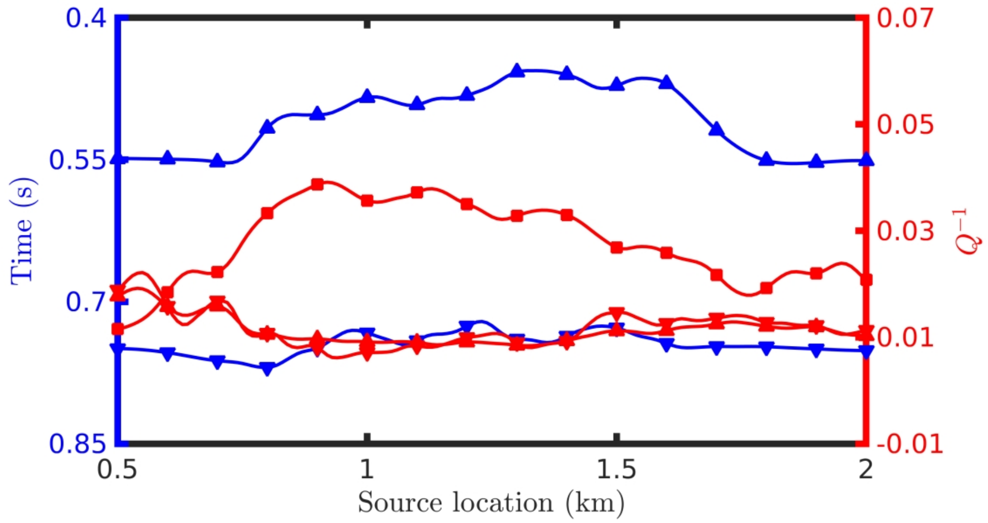

Figure 19d. Zero-offset inversion results for match-filter-based attenuated traveltime estimation ((a), (c)) and piecewise linear regression ((b), (d)). (a) and (b) are obtained from seismograms with Gaussian random noise of σ_n = 0.005; (c) and (d) are obtained from seismograms with Gaussian random noise of σ_n = 0.01.

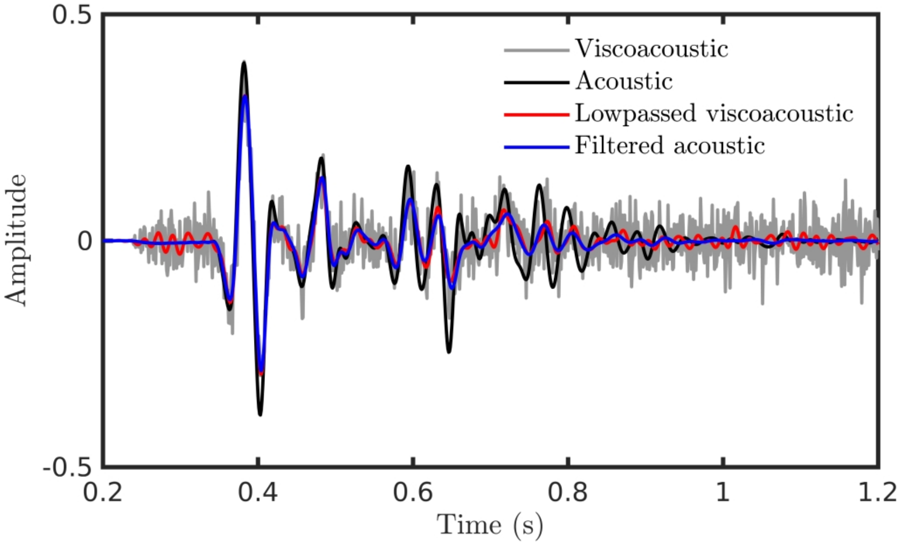

Figure 20a. Sample trace inversion results for match-filter-based attenuated traveltime estimation ((a), (c)) and piecewise linear regression ((b), (d)) at x_s = 1300 m, x_r = 1300 m. (a) and (b) are obtained from seismograms with Gaussian random noise of σ_n = 0.005; (c) and (d) are obtained from seismograms with Gaussian random noise of σ_n = 0.01.

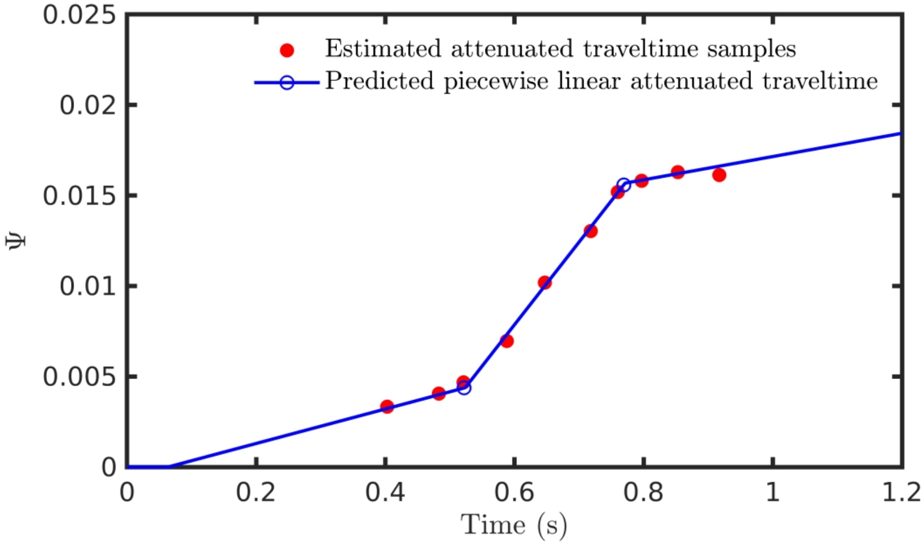

Figure 20b. Sample trace inversion results for match-filter-based attenuated traveltime estimation ((a), (c)) and piecewise linear regression ((b), (d)) at x_s = 1300 m, x_r = 1300 m. (a) and (b) are obtained from seismograms with Gaussian random noise of σ_n = 0.005; (c) and (d) are obtained from seismograms with Gaussian random noise of σ_n = 0.01.

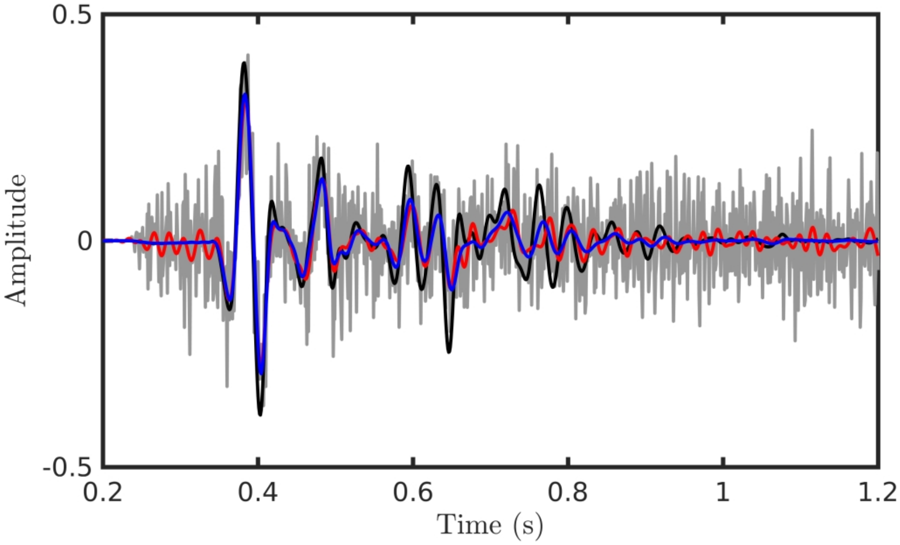

Figure 20c. Sample trace inversion results for match-filter-based attenuated traveltime estimation ((a), (c)) and piecewise linear regression ((b), (d)) at x_s = 1300 m, x_r = 1300 m. (a) and (b) are obtained from seismograms with Gaussian random noise of σ_n = 0.005; (c) and (d) are obtained from seismograms with Gaussian random noise of σ_n = 0.01.

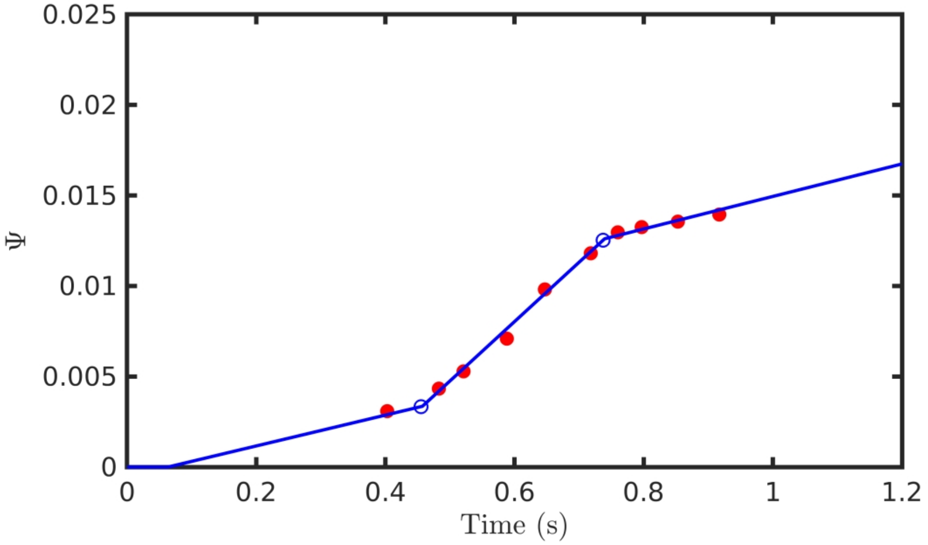

Figure 20d. Sample trace inversion results for match-filter-based attenuated traveltime estimation ((a), (c)) and piecewise linear regression ((b), (d)) at x_s = 1300 m, x_r = 1300 m. (a) and (b) are obtained from seismograms with Gaussian random noise of σ_n = 0.005; (c) and (d) are obtained from seismograms with Gaussian random noise of σ_n = 0.01.

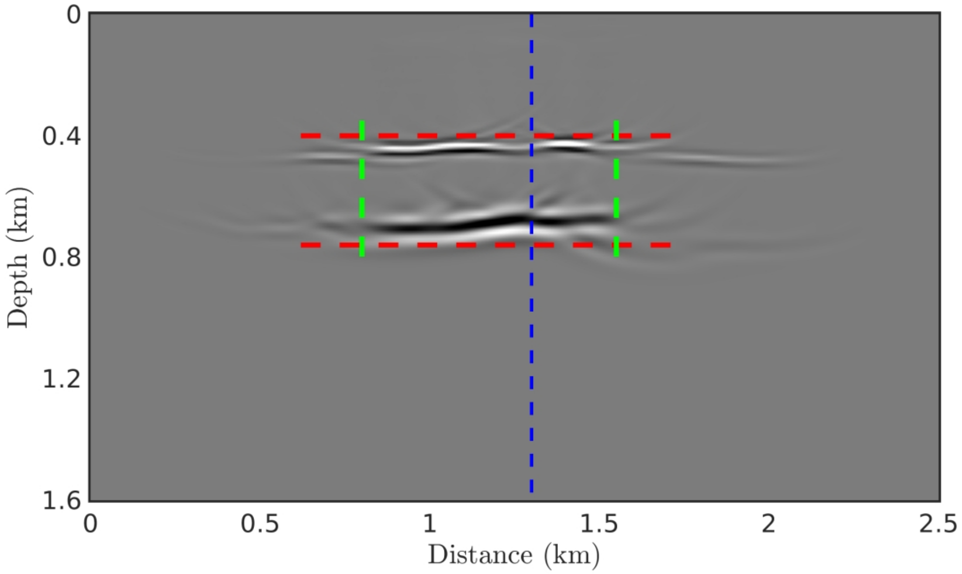

Figure 21a. Q-interface images obtained from seismograms with Gaussian random noise (a) σ_n = 0.005 and (b) 0.01. The red and green dashed lines approximately mark the vertical and horizontal ranges of the Q anomaly. The blue dashed lines indicate the position of the sampled trace shown in Figure 17.

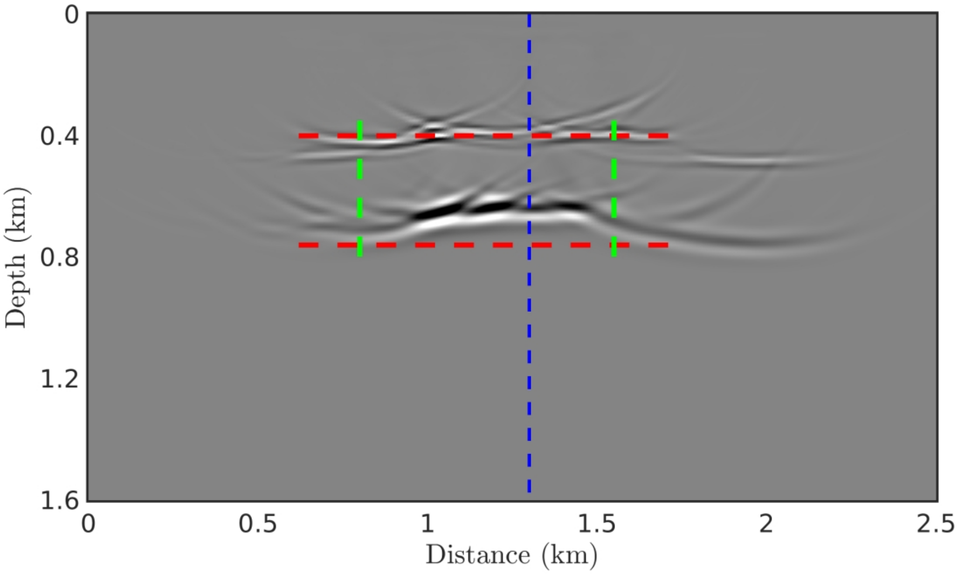

Figure 21b. Q-interface images obtained from seismograms with Gaussian random noise (a) σ_n = 0.005 and (b) 0.01. The red and green dashed lines approximately mark the vertical and horizontal ranges of the Q anomaly. The blue dashed lines indicate the position of the sampled trace shown in Figure 17.

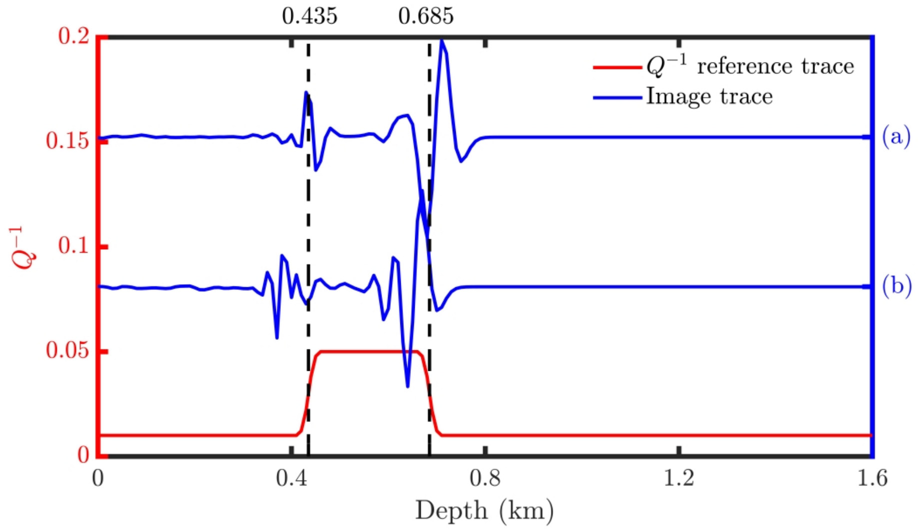

Figure 22. Comparison between Q-interface image traces with the reference Q model. (a) and (b) represent the image traces sampled from Figure 21a and 21b, respectively.

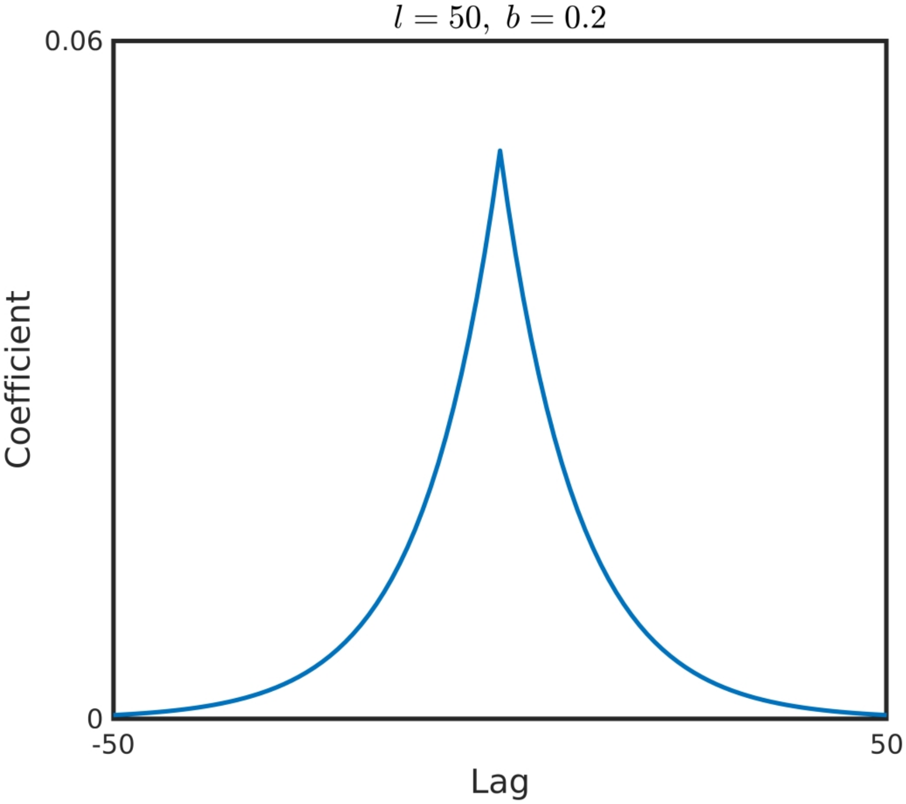

Figure B-1a. The 1-D smoothers used in the match-filter-based waveform inversion and piecewise linear regression: (a)-(c) are smoothers for the layered-model example along t, x_r and x_s directions, respectively; and (d)-(f) are smoothers for the gas-chimney-model example along t, x_r and x_s directions, respectively.

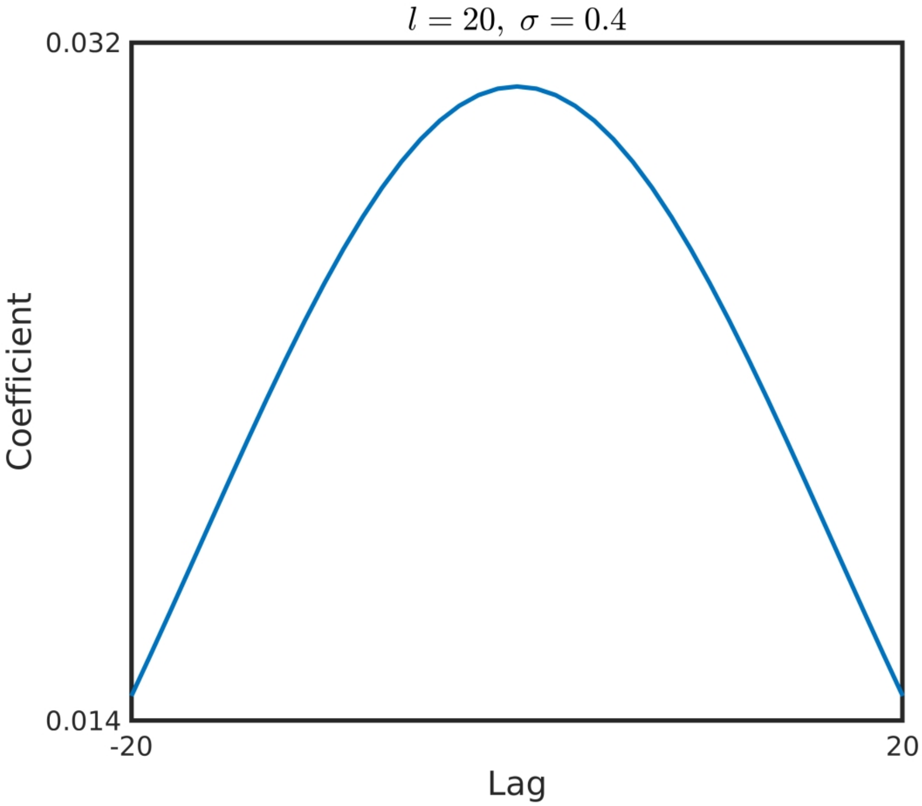

Figure B-1b. The 1-D smoothers used in the match-filter-based waveform inversion and piecewise linear regression: (a)-(c) are smoothers for the layered-model example along t, x_r and x_s directions, respectively; and (d)-(f) are smoothers for the gas-chimney-model example along t, x_r and x_s directions, respectively.

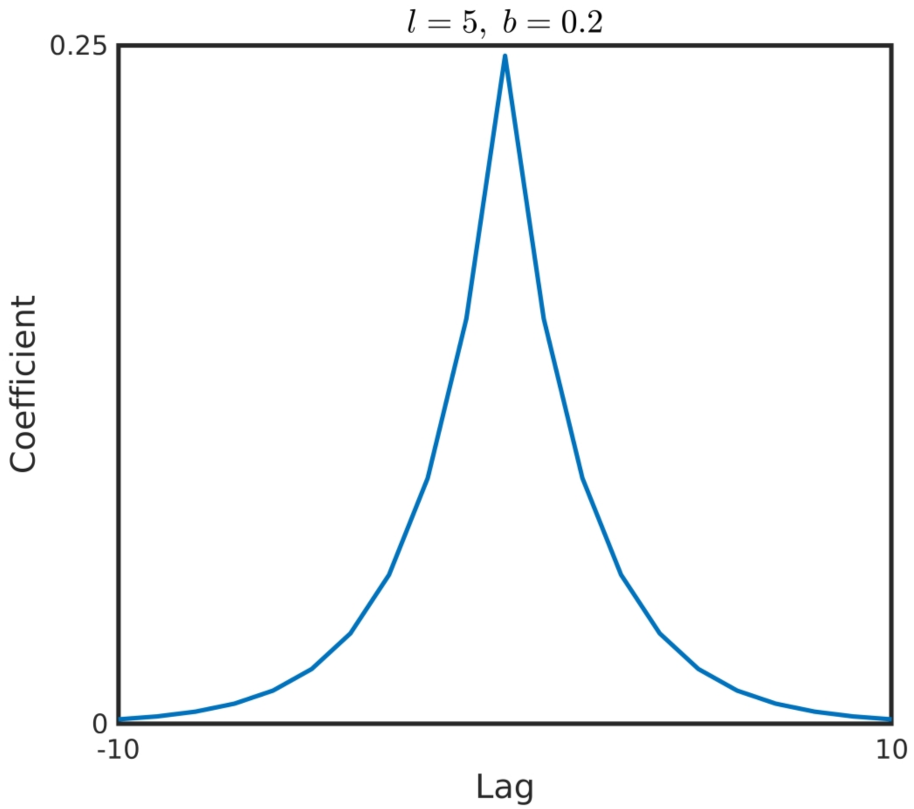

Figure B-1c. The 1-D smoothers used in the match-filter-based waveform inversion and piecewise linear regression: (a)-(c) are smoothers for the layered-model example along t, x_r and x_s directions, respectively; and (d)-(f) are smoothers for the gas-chimney-model example along t, x_r and x_s directions, respectively.

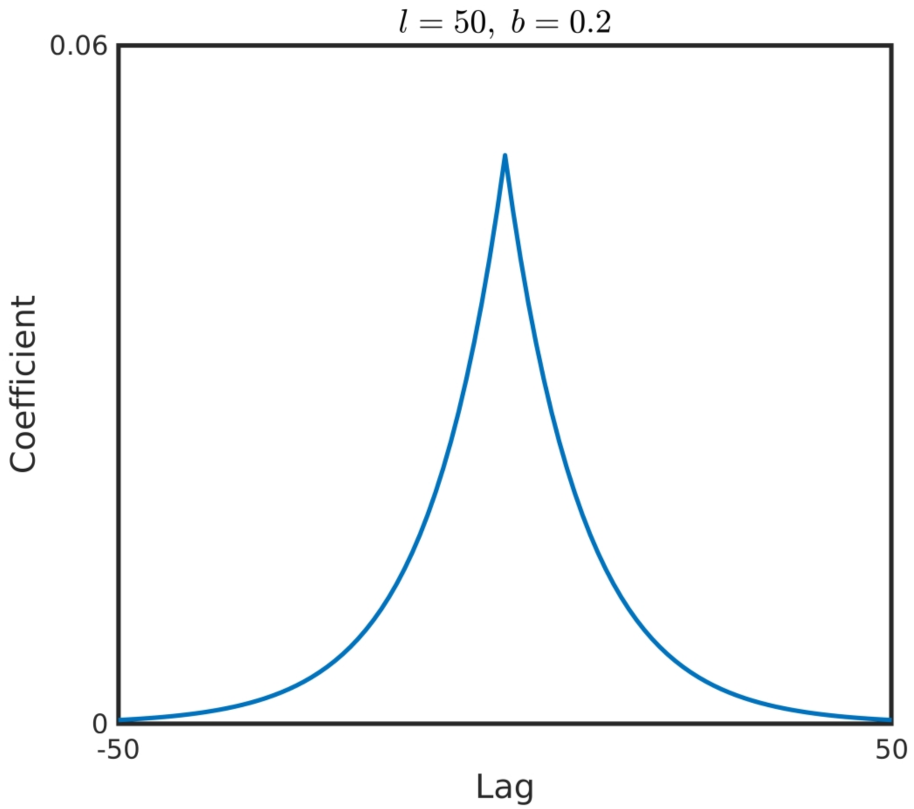

Figure B-1d. The 1-D smoothers used in the match-filter-based waveform inversion and piecewise linear regression: (a)-(c) are smoothers for the layered-model example along t, x_r and x_s directions, respectively; and (d)-(f) are smoothers for the gas-chimney-model example along t, x_r and x_s directions, respectively.

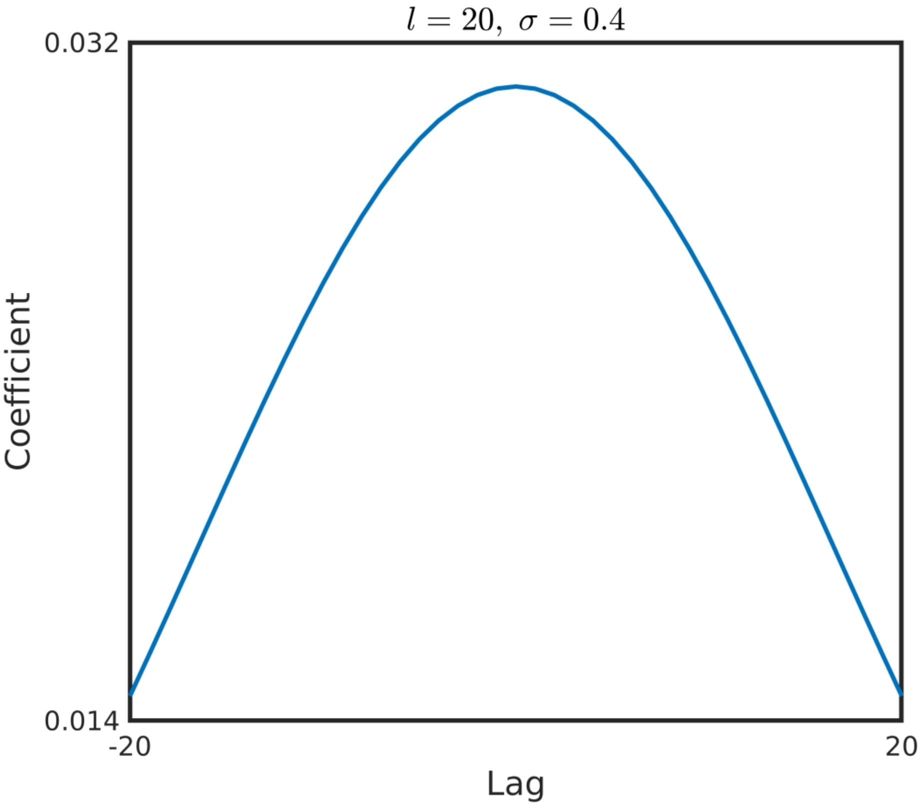

Figure B-1e. The 1-D smoothers used in the match-filter-based waveform inversion and piecewise linear regression: (a)-(c) are smoothers for the layered-model example along t, x_r and x_s directions, respectively; and (d)-(f) are smoothers for the gas-chimney-model example along t, x_r and x_s directions, respectively.

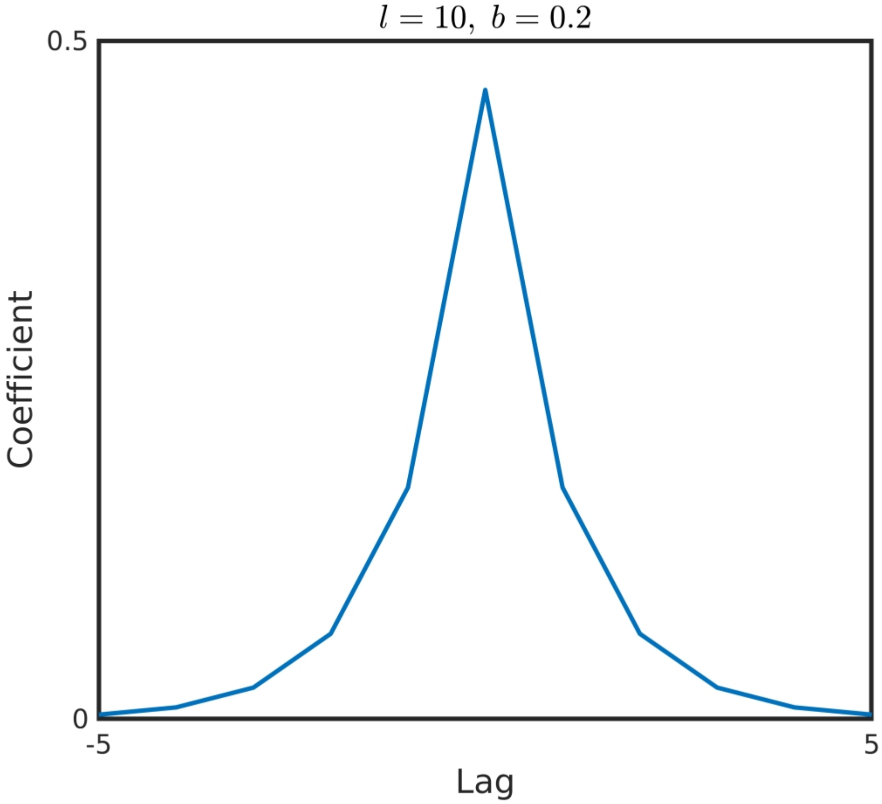

Figure B-1f. The 1-D smoothers used in the match-filter-based waveform inversion and piecewise linear regression: (a)-(c) are smoothers for the layered-model example along t, x_r and x_s directions, respectively; and (d)-(f) are smoothers for the gas-chimney-model example along t, x_r and x_s directions, respectively.

	Layered model	Gas chimney model
Model Grids	201×201	161×251
Grid Intervals (m)	10	10
Total Sources	81	151
First Source Location (m)	$(200, 100)$	$(500, 100)$
Source Spacing (m)	20	10
Total Receivers	201	251
First Receiver Location (m)	$(0, 50)$	$(0, 50)$
Receiver Spacing (m)	10	10
Total Recording time (s)	1.6	1.5
Time sampling Rate (ms)	1	1
Wavelet Peak Frequency (Hz)	25	25
Velocity Reference Frequency (Hz)	100	100

Table 1: Model discretizations and acquisation geometry configurations.

DATA AND MATERIALS AVAILABILITY

Data associated with this research are available and can be obtained by contacting the corresponding author.

DOI:10.1190/geo2019-0759.1